

Discrete-vortex method with novel shedding criterion for unsteady aerofoil flows with intermittent leading-edge vortex shedding

Kiran Ramesh^{1,†}, Ashok Gopalarathnam¹, Kenneth Granlund²,
Michael V. Ol² and Jack R. Edwards¹

¹Department of Mechanical and Aerospace Engineering, North Carolina State University, Raleigh, NC 27695-7910, USA

²US Air Force Research Laboratory, Air Vehicles Directorate, AFRL/RBAL, Building 45, 2130 8th Street, WPAFB, OH 45433, USA

(Received 18 November 2013; revised 15 May 2014; accepted 21 May 2014;
first published online 23 June 2014)

Unsteady aerofoil flows are often characterized by leading-edge vortex (LEV) shedding. While experiments and high-order computations have contributed to our understanding of these flows, fast low-order methods are needed for engineering tasks. Classical unsteady aerofoil theories are limited to small amplitudes and attached leading-edge flows. Discrete-vortex methods that model vortex shedding from leading edges assume continuous shedding, valid only for sharp leading edges, or shedding governed by *ad-hoc* criteria such as a critical angle of attack, valid only for a restricted set of kinematics. We present a criterion for intermittent vortex shedding from rounded leading edges that is governed by a maximum allowable leading-edge suction. We show that, when using unsteady thin aerofoil theory, this leading-edge suction parameter (LESP) is related to the A_0 term in the Fourier series representing the chordwise variation of bound vorticity. Furthermore, for any aerofoil and Reynolds number, there is a critical value of the LESP, which is independent of the motion kinematics. When the instantaneous LESP value exceeds the critical value, vortex shedding occurs at the leading edge. We have augmented a discrete-time, arbitrary-motion, unsteady thin aerofoil theory with discrete-vortex shedding from the leading edge governed by the instantaneous LESP. Thus, the use of a single empirical parameter, the critical-LESP value, allows us to determine the onset, growth, and termination of LEVs. We show, by comparison with experimental and computational results for several aerofoils, motions and Reynolds numbers, that this computationally inexpensive method is successful in predicting the complex flows and forces resulting from intermittent LEV shedding, thus validating the LESP concept.

Key words: computational methods, separated flows, vortex interactions

1. Introduction

Unsteady flow phenomena are prevalent in a wide range of problems in nature and engineering. These include, but are not limited to, dynamic stall in rotorcraft and wind turbines, leading-edge vortices in delta-wings, micro air vehicle (MAV) design,

† Email address for correspondence: kramesh2@ncsu.edu

gust handling and flow control. Unsteady flows are characterised by rapid changes in the circulation of the aerofoil, apparent-mass effects, flow separation and vortices in the flow field. Theoretical work on these topics dates back to the 1920s and 1930s. Theodorsen (1935) developed a potential flow solution for the unsteady airloads on a flat plate undergoing harmonic, small-amplitude oscillations in pitch and plunge. Wagner (1925) solved for the lift response of an aerofoil undergoing a step change in angle of attack (indicial response). The unsteady lift coefficient due to arbitrary changes in angle of attack could hence be calculated by superposition using the Duhamel integral (Leishman 2002, chapter 8). McCune, Lam & Scott (1990) have presented a nonlinear theory of unsteady potential flow which allows determination of lift and moment coefficients for large-amplitude motions.

Although these and other classical theories (Garrick 1937; von Kármán & Sears 1938) have proven invaluable in offering insight into unsteady aerodynamics and in fields such as aeroelasticity, their applicability in many problems is hindered by their inherent assumptions (small amplitudes, planar wake, fully attached flow). Advances in computational fluid dynamics (CFD) and experimental techniques have facilitated the detailed study and analysis of unsteady phenomena. Ol *et al.* (2009a) and McGowan *et al.* (2011) have analysed the forces and flow fields for unsteady motions over a broad parameter space using both experimental and computational methods. Garmann & Visbal (2011) and Granlund, Ol & Bernal (2013) have investigated pitching flat plates in detail through computational and experimental methods respectively. Baik *et al.* (2012), Pitt Ford & Babinsky (2013) and Rival *et al.* (2014) have studied the effects and influence of leading-edge vortices using experimental techniques. However, these methods are not suitable for applications such as real-time simulation, rapid analysis, control and design, because of cost and time considerations. Since closed-form solutions from theory are incapable of capturing the various nonlinear effects, we may suitably augment theory with numerical procedures to expand its range of applicability. Brunton, Rowley & Williams (2013) and Wang & Eldredge (2013) have developed such phenomenologically augmented theoretical methods. With computing power and technology advancing rapidly, low-order numerical models (constructed by augmenting classical theory) may provide the perfect balance between fidelity and cost. In this paper, a discrete-vortex method with a novel shedding criterion is proposed for modelling of massively separated, vortex-dominated flows.

Significant investigation of unsteady flow phenomena has been carried out by researchers interested in studying and finding methods to suppress dynamic stall. Dynamic stall refers to unsteady separation and stall phenomena on aerofoils that execute time-dependent motion, where the effective angle of attack exceeds the static stall angle (McCroskey 1981, 1982). This process results in a delayed onset of flow separation/stall, followed by the shedding of a vortex from the leading edge of the aerofoil which traverses the aerofoil chord (Leishman 2002, chapter 9). Although this vortex enhances the lift when it stays over the surface of the aerofoil, it also creates large nose-down pitching moments and flow separation over the entire aerofoil when it convects off the trailing edge. Hence dynamic stall can lead to violent vibrations and dangerously high airloads, resulting in material fatigue and structural failure. A good review of experimental and numerical approaches toward understanding and predicting dynamic stall is given by Carr (1988) and Carr *et al.* (1990). A large number of semi-empirical methods have been developed to model dynamic stall for use in rotor analysis and design. A brief description of some of these models, along with a demonstration of their capabilities is given in Leishman (2002, chapter 9). These models however, rely on several empirical parameters and can only be used in conditions that are bounded by validation with experimental data.

Discrete-vortex methods have also been used extensively to model unsteady separated flows. These methods are typically based on potential-flow theory, and the shear layers representing separated flow emanate from the surface in the form of discrete vortices. Clements & Maull (1975) and Saffman & Baker (1979) provide detailed background on the historical development of the discrete-vortex method. A review of more recent progress on the application of vortex methods for flow simulation is given by Leonard (1980). Clements (1973), Sarpkaya (1975), Kiya & Arie (1977), and other researchers have applied this category of methods successfully to model flow past inclined plates and bluff bodies. Katz (1981) has developed a method for partially separated flow past an aerofoil, where the location of separation on the aerofoil has to be known through experiment or other means. More recently, low-order methods based on discrete vortices have been developed by Ansari, Żbikowski & Knowles (2006a), Wang & Eldredge (2013), Xia & Mohseni (2013), and Hammer, Altman & Eastep (2014) to model leading-edge vortices in unsteady flows, with applications to insect flight and MAV aerodynamics. Although these methods are based on potential theory, they capture the essential physics in flows of interest by augmentation of inviscid theory with discrete-vortex shedding. Apart from providing a means to calculate the force coefficients on the aerofoil, these methods also enable study of the flow features and identification of dominant unsteady effects which require further modelling. These are significant advantages of this class of methods over semi-empirical methods, which only allow determination of the force coefficients through empirical fitting. However, the computational complexity increases as $O(n^2)$ (when fast summation methods are not used), where n is the number of vortices in the flow field, resulting in possibly large computing times. Moreover, the methods cited above assume some *ad-hoc* start and stop criteria for vortex shedding, such as continuous shedding from a given location (valid only for sharp edges) or shedding that starts and stops depending on whether the local angle of attack exceeds a critical value (valid only for a small range of motions). A more general vortex shedding criterion is needed to make discrete-vortex methods broadly applicable to a wide range of geometries (including aerofoils with rounded leading edges) and arbitrary unsteady motions.

In previous research (Ramesh *et al.* 2013b), the authors have developed an unsteady aerofoil theory based on potential flow, which holds uniformly regardless of amplitude and reduced frequency of motion, and shape of trailing wake. This method was applied to a pitch-up, hold, pitch-down motion which was characterised by the shedding of a strong leading-edge vortex (LEV) during a part of the motion. The method was seen to predict well even under conditions of large amplitude and high reduced frequency except during the portions when the LEV dominates the flow. To successfully model flows with leading-edge vortices, a method to predict the onset of LEV formation was required. With this objective, the leading-edge suction parameter (LESP) was developed by the authors (Ramesh *et al.* 2011). This parameter is a measure of the suction at the leading edge and it was shown that initiation of LEV formation always occurred at the same critical value of LESP, regardless of motion kinematics so long as the aerofoil and Reynolds number of operation were the same. These methods are reviewed in § 2.1. In this research, a discrete-vortex method is proposed in which the LESP criterion is used to modulate the initiation, growth, and termination of intermittent LEV shedding. The extension of the LESP criterion to handle LEV shedding and termination is discussed in § 2.2. Details of the vortex method are discussed in § 2.3. The LESP-modulated discrete-vortex method (LDVM) from the current work is validated for use in LEV-dominated flows against results from CFD and experiment in § 3. Limitations of the method and possible extensions are briefly discussed in § 4.

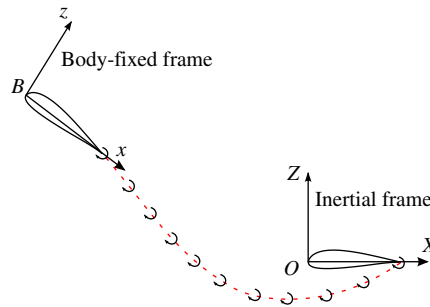


FIGURE 1. (Colour online) An illustration of the time-stepping method.

2. LESP-modulated discrete-vortex method (LDVM)

2.1. Background

In this section, the theoretical methods developed previously by the authors are summarised. The interested reader may refer to Ramesh *et al.* (2011) and Ramesh *et al.* (2013*b*) for further details.

2.1.1. Large-angle unsteady thin-aerofoil theory

The large-angle unsteady thin-aerofoil theory was developed with an aim of eliminating the traditional small-angle assumptions in thin-aerofoil theory which are invalid in flows of current interest. This method builds on the time-stepping approach given by Katz & Plotkin (2000). In figure 1, the inertial frame is given by *OXYZ* and the body frame, attached to the moving aerofoil, by *Bxyz*. At time $t = 0$, the two frames coincide and at time $t > 0$, the body frame moves toward the left of the page along a time-varying path. At each time step, a discrete trailing-edge vortex (TEV) is shed from the trailing edge.

Analogous to classical thin-aerofoil theory, the vorticity distribution over the aerofoil, $\gamma(x)$, is taken to be a Fourier series,

$$\gamma(\theta, t) = 2U \left[A_0(t) \frac{1 + \cos \theta}{\sin \theta} + \sum_{n=1}^{\infty} A_n(t) \sin(n\theta) \right], \quad (2.1)$$

where θ is a variable of transformation related to the chordwise coordinate x as

$$x = \frac{c}{2}(1 - \cos \theta), \quad (2.2)$$

and in which $A_0(t)$, $A_1(t)$, \dots , $A_n(t)$ are the time-dependent Fourier coefficients, c is the aerofoil chord, and U is the component of the aerofoil velocity in the negative X direction. The Kutta condition (zero vorticity at the trailing edge) is enforced implicitly through the form of the Fourier series. The Fourier coefficients are determined as a function of the instantaneous local downwash on the aerofoil by enforcing the boundary condition that the flow must remain tangential to the aerofoil surface,

$$A_0(t) = -\frac{1}{\pi} \int_0^\pi \frac{W(x, t)}{U} d\theta, \quad (2.3)$$

$$A_n(t) = \frac{2}{\pi} \int_0^\pi \frac{W(x, t)}{U} \cos n\theta d\theta. \quad (2.4)$$

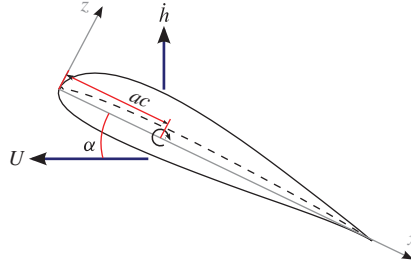


FIGURE 2. (Colour online) Aerofoil velocities (positive as shown) and pivot location.

The induced velocity normal to the aerofoil surface, $W(x, t)$, henceforth referred to as downwash, is calculated from components of motion kinematics, depicted in figure 2, and induced velocities from vortices in the flow field:

$$W(x, t) \equiv \frac{\partial \phi_B}{\partial z} = \frac{\partial \eta}{\partial x} \left(U \cos \alpha + \dot{h} \sin \alpha + \frac{\partial \phi_{lev}}{\partial x} + \frac{\partial \phi_{tev}}{\partial x} \right) - U \sin \alpha - \dot{\alpha}(x - ac) + \dot{h} \cos \alpha - \frac{\partial \phi_{tev}}{\partial z} - \frac{\partial \phi_{lev}}{\partial z} \quad (2.5)$$

where ϕ_B , ϕ_{lev} and ϕ_{tev} are the velocity potentials associated with bound, leading-edge and trailing-edge vorticity, $\eta(x)$ is the camber distribution on the aerofoil, $\partial \phi_{lev}/\partial x$ and $\partial \phi_{tev}/\partial x$ are velocities induced tangential to the chord by leading- and trailing-edge discrete vortices and $\partial \phi_{lev}/\partial z$ and $\partial \phi_{tev}/\partial z$ are induced velocities normal to the chord. The motion parameters include the plunge velocity in the Z direction, \dot{h} , and the pitch angle of the chord with respect to the X direction, α . The LEV shedding process is detailed in § 2.2. TEVs are shed at every time step as mentioned earlier, and their strengths are calculated iteratively such that Kelvin's circulation condition is enforced:

$$\Gamma_b(t) + \sum_{m=1}^{N_{lev}} \Gamma_{tev_m} + \sum_{n=1}^{N_{lev}} \Gamma_{lev_n} = 0 \quad (2.6)$$

where Γ_b is the bound circulation calculated by integrating the chordwise distribution of bound vorticity over the aerofoil chord:

$$\Gamma_b = Uc\pi \left[A_0(t) + \frac{A_1(t)}{2} \right]. \quad (2.7)$$

2.1.2. *LESP criterion for initiation of LEV formation*

It has been known for several decades that the onset of separation at the leading edge is governed by criticality of flow parameters at the leading edge. Evans & Mort (1959) have shown that leading-edge separation is directly related to the strong adverse pressure gradient that follows the suction peak at the leading edge. Beddoes (1978) has shown an equivalent correspondence between leading-edge separation and the flow velocity at the leading edge. Jones & Platzer (1997) have studied the onset of laminar separation at the leading edge for a pitching NACA 0012 aerofoil as an indication of the initiation of dynamic stall. They showed that the angle of attack at

which the laminar separation first occurs increases with pitch rate. This result was shown to be in qualitative agreement with experiments of Chandrasekhara, Ahmed & Carr (1990, 1993). More interestingly, at the angle of attack corresponding to the first occurrence of laminar separation at the leading edge, the leading-edge flows (pressure distributions, pressure-gradient distributions, and locations of stagnation and laminar-separation points) were found to be invariant with pitch rate (see Ekaterinaris & Platzer 1998). Inspired by these works, we sought to develop a criterion to predict the initiation of LEV formation in unsteady flows. The objective was that this criterion would be based on some inviscid parameter, termed the LESP in Ramesh *et al.* (2011), which can be determined at every time step of the unsteady thin-aerofoil theory.

Using an inviscid parameter to predict trends in viscous behaviour is not a new idea. For example, it has long been known that the ideal lift coefficient of a laminar-flow aerofoil in steady flow, which usually falls close to the middle of the drag bucket, corresponds to the lift coefficient at which the A_0 coefficient is zero (see Theodorsen 1931; Abbott & von Doenhoff 1959). This idea can be used to estimate the change in C_l of the middle of the drag bucket due to a trailing-edge cruise flap (McAvoy & Gopalarathnam 2002). The A_0 term in thin-aerofoil theory is the only term that results in a singularity in the vorticity distribution at the leading edge, and hence is a good measure of the flow at the leading edge. We hypothesized in Ramesh *et al.* (2011) that the LESP would be connected to the A_0 Fourier term and that a critical value of this LESP would correspond to onset of LEV formation.

In thin-aerofoil theory, the aerofoil thickness and hence the leading-edge radius is zero. This requires the flow to turn 180° around the leading edge, giving rise to a theoretically infinite flow velocity at the leading edge, V_{LE} , of a thin aerofoil. From Garrick (1937) and von Kármán & Burgers (1963), we have that the form of this theoretically infinite velocity is given by

$$V_{LE}(t) = \lim_{x \rightarrow LE} \frac{S}{\sqrt{x}} \tag{2.8}$$

where S is a measure of the suction at the leading edge and is given by

$$S = \lim_{x \rightarrow LE} \frac{1}{2} \gamma(x, t) \sqrt{x}. \tag{2.9}$$

Since $\gamma(x, t)$ (though infinite at the leading edge) is proportional to $1/\sqrt{(x)}$, the value of S is finite. Evaluating using the current formulation,

$$S = \sqrt{c}UA_0(t). \tag{2.10}$$

Because the LESP is a non-dimensional measure of the suction at the leading edge, S , for given values of c and U , we may simply equate it to the A_0 value as

$$LESP(t) = A_0(t). \tag{2.11}$$

As proposed by Katz (1981), real aerofoils have rounded leading edges which can support some suction even when the stagnation point is away from the leading edge. The amount of suction that can be supported is a characteristic of the aerofoil shape and Reynolds number of operation. Since the LESP (the A_0 value) is a measure of the suction/velocity at the leading edge, it was a logical choice to base the criterion for initiation of LEV formation on the LESP. To understand the connection between the LESP and the initiation of LEV formation, we examined in Ramesh *et al.* (2011)

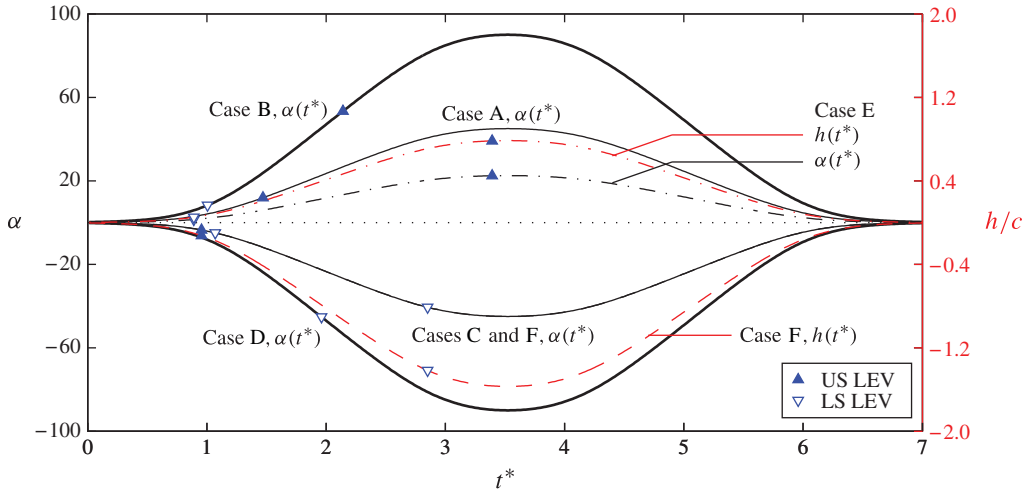


FIGURE 3. (Colour online) Variation with $t^* = tU/c$ of $\alpha(t^*)$ and $h/c(t^*)$ for cases A–F, with instants of LEV initiation marked.

Case	α_{\max} (deg.)	K_α	Pivot (x_p/c)	$(h/c)_{\max}$	K_h
A	45	0.2	0	—	—
B	90	0.4	1.0	—	—
C	-45	0.2	0	—	—
D	-90	0.4	1.0	—	—
E	22.5	0.1	0.5	0.79	0.2
F	-45	0.2	0.5	-1.57	0.4

TABLE 1. Motion kinematics for demonstrating the LESP criterion using computational data.

and Ramesh (2013) the value of LESP at the initiation of LEV formation for several motions. A subset of this study, from Ramesh (2013), is presented in the discussion below in which the SD7003 aerofoil was used at a free-stream Reynolds number of 100 000.

Table 1 lists six motion kinematics of varying amplitudes, frequencies, and pivot locations which evinced formation of one or more leading-edge vortices. The Eldredge function (Eldredge, Wang & Ol 2009; Wang & Eldredge 2013) described in appendix B, with a smoothing parameter $a = 2$, is used to generate these kinematics. The first four kinematics comprise pitching motion alone while the last two are combinations of pitch and plunge. In figure 3, the motion kinematics for all the cases are co-plotted and the time instants corresponding to initiation of LEV formation, as determined from CFD using the procedure detailed in appendix A, are marked on the curves. Clearly, there is no obvious relation between initiation of LEV formation and the values of pitch or plunge at that time instant. These results confirm that it is not possible to formulate a general criterion for LEV initiation in unsteady flow using a critical value of a kinematic parameter such as pitch angle. In figure 4, the time variation of LESP for the six motions from unsteady thin aerofoil theory are co-plotted with the instants of LEV formation marked. It is seen that the initiation

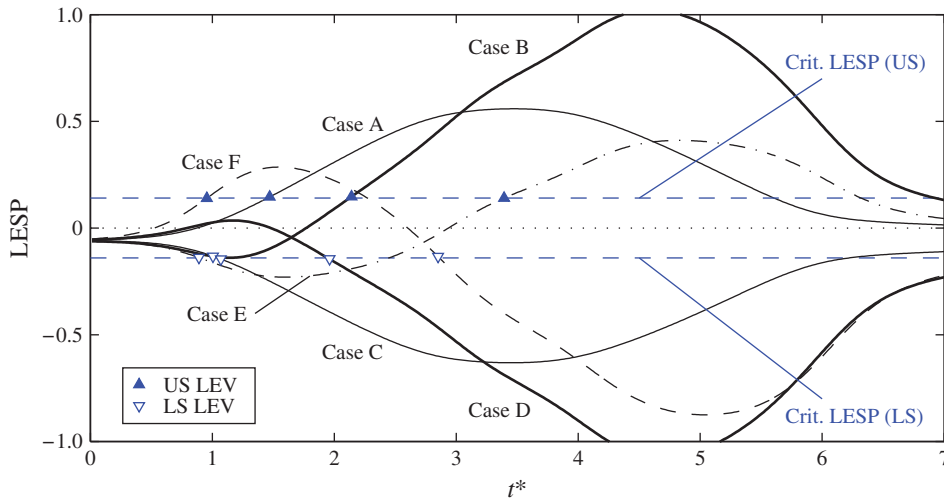


FIGURE 4. (Colour online) Variation with $t^* = tU/c$ of LESP for cases A–F, with instants of LEV initiation marked. US denotes upper surface, and LS lower surface.

of upper-surface LEV formation occurs at a constant LESP value, which is $+0.14$ in this case, and the initiation of the lower-surface LEVs occurs at a constant LESP, which is -0.14 .

These results demonstrate that there is critical value of LESP for a given aerofoil and Reynolds number above which LEV formation is initiated, regardless of motion kinematic parameters such as amplitude, reduced frequency, and pivot location. For the example just considered, the critical value is 0.14 . The instantaneous LESP value (the A_0 coefficient) exceeding the critical LESP value (function of aerofoil and Reynolds number) marks the initiation of LEV formation as predicted by this method. The sign of the instantaneous LESP indicates the surface of the aerofoil on which LEV forms (positive for upper surface, negative for lower surface).

The recent research of Morris & Rusak (2013) on inception of leading-edge stall on stationary, two-dimensional, smooth, thin aerofoils provides another explanation of why the critical value of the A_0 term should correspond to initiation of LEV formation. In their work, the authors have used matched asymptotic theory with the flow around most of the aerofoil chord described in terms of an outer region which is solved using thin-aerofoil theory. The flow in the vicinity of the leading edge forms the inner region, which is treated as a model problem of a uniform, incompressible and viscous flow past a semi-infinite parabola and solved through numerical simulations of the unsteady Navier–Stokes equations. The flows in the inner and outer regions are made to asymptotically match each other. The far-field circulation for the inner flow is governed by a parameter that is related to the aerofoil angle of attack. This approach allows the determination of the critical angle of attack for leading-edge stall onset as the condition at which a global separation zone is predicted in the solution for the inner flow. For a given aerofoil geometry, the A_0 value is linearly related to the angle of attack in stationary flow. This shows that, at a given Reynolds number, leading-edge stall in stationary aerofoil flow is related to a critical value of the A_0 coefficient. In the current unsteady thin-aerofoil theory, the A_0 value accounts not only for the instantaneous angle of attack, but also for the motion kinematics and the effect of vorticity in the flow through the zero-normal-flow boundary conditions in (2.5).

It follows, therefore, that the critical value of A_0 would correspond to initiation of LEV formation in unsteady flow.

2.2. LEV shedding and termination criteria

Expanding on the critical-LESP criterion for initiation of LEV formation in § 2.1.2, we further postulate that even during the LEV shedding process, the leading-edge suction is limited to the critical value. This assumption is based on the argument that rounded leading edges will support a certain maximum amount of suction, even when the leading-edge flow is separated (Katz 1981). Thus, as long as the motion and/or the vortical structures in the flow attempt to cause the leading-edge suction to exceed the critical value, the leading edge limits the suction to the critical value by shedding leading-edge vorticity at the appropriate rate.

In the discrete-vortex method employed in this paper, TEV are shed at every time step and their strengths are determined by enforcing Kelvin's circulation condition as described in § 2.1. Leading-edge discrete vortices are shed when the instantaneous LESP value (monitored at each time step) is higher than the critical LESP value, which is empirically pre-determined for the given aerofoil and Reynolds number using data from experiment or CFD for a single prototypical motion. The strength of the leading-edge discrete vortex at any time instant is determined such that the instantaneous LESP value, which would have otherwise exceeded the critical LESP value, is made equal to the latter. With this criterion, the direction of the discrete vortex shed at the leading edge is automatically determined: clockwise or counterclockwise depending on whether the LESP is positive or negative. The discrete vortices are convected with the local velocity like in other discrete-vortex methods. When the instantaneous LESP falls below the critical value, then LEV shedding is terminated. Thus, with the use of a single empirically-determined parameter, the critical LESP, the approach is able to account for the initiation, shedding, and termination of intermittent LEVs in an arbitrary unsteady motion.

2.3. Implementation of the discrete-vortex method

The earliest discrete-vortex methods used point vortices to represent flows (Rosenhead 1932). However, this method could lead to vortices in close proximity inducing artificially large velocities on each other. Also, small disturbances which are inherent in numerical methods may lead to non-smooth solutions. Chorin (1973) introduced the idea of using vortex blobs with finite core radii, which had more realistic vorticity distributions and bounded induced velocities in the flow field. Hald (1979) proved that the vortex-blob method was convergent so long as the vortex-core radius was larger than the average spacing between vortices. In other words, it is necessary that adjacent vortices overlap for convergence of the method. In the present method, the vortex-core model proposed by Vatisas, Kozel & Mih (1991) is used, which gives an excellent approximation to the Lamb–Oseen vortex. Using Vatisas's vortex model with order 2 and using v_{core} to denote the vortex-core radius, we have that the induced velocities (u and w) by the k th vortex in the X and Z direction are:

$$u = \frac{\gamma_k}{2\pi} \frac{Z - Z_k}{\sqrt{((X - X_k)^2 + (Z - Z_k)^2) + v_{core}^4}}, \quad (2.12)$$

$$w = -\frac{\gamma_k}{2\pi} \frac{X - X_k}{\sqrt{((X - X_k)^2 + (Z - Z_k)^2) + v_{core}^4}}. \quad (2.13)$$

A non-dimensional time step ($\Delta t^* = \Delta t U/c$) of 0.015 is used for the simulations presented in this paper. The average spacing between the vortices, d , is calculated as:

$$d = U \Delta t = c \Delta t^*. \tag{2.14}$$

Using guidelines from Leonard (1980), the vortex core radius is taken to be 1.3 times the average spacing between the vortices,

$$\frac{v_{core}}{c} = 1.3 \Delta t^* = 0.02. \tag{2.15}$$

Discrete-vortex methods traditionally position the last shed vortex along the path of the shedding edge (Katz 1981). In the current method, the placement methodology given by Ansari *et al.* (2006a) and Ansari, Żbikowski & Knowles (2006b) is used, where the latest vortex is placed at one-third of the distance from the shedding edge to the previously shed vortex. This method takes into account both the aerofoil motion and the convection of the previous shed vortex, thereby describing the flow more accurately:

$$(X, Z)_{lev_i/lev_i} = (X, Z)_{TE/LE} + \frac{1}{3}((X, Z)_{lev_{i-1}/lev_{i-1}} - (X, Z)_{TE/LE}). \tag{2.16}$$

The position of the first shed vortex is determined using the velocity at the shedding edge. It is noted that TEVs are shed at every time step but leading-edge vortices are shed only when the LESP criterion dictates it. Hence the position of the first shed vortex is calculated only once at the trailing edge but may be calculated on multiple occasions at the leading edge when intermittent LEV shedding occurs.

At each time step, all the free vortices in the flow field are convected by the net local velocity induced at their centres. A first-order time-stepping procedure is used, since no change in accuracy was observed by using higher-order methods.

2.4. Pressure distribution, forces and moment on the aerofoil

From the unsteady Bernoulli’s equation, we have that:

$$\Delta p(x) = p_l(x) - p_u(x) \tag{2.17}$$

$$= \rho \left(\frac{1}{2}(V_u^2 - V_l^2) + \left(\frac{\partial \phi}{\partial t} \right)_u - \left(\frac{\partial \phi}{\partial t} \right)_l \right). \tag{2.18}$$

The velocity potential is comprised of components from bound vorticity, LEVs and TEVs:

$$\phi = \phi_b + \phi_{lev} + \phi_{tev} \tag{2.19}$$

and the tangential velocities on the upper and lower surface are expressed as:

$$V_u = U \cos \alpha + \dot{h} \sin \alpha + \left(\frac{\partial \phi_{lev}}{\partial x} \right)_u + \left(\frac{\partial \phi_{tev}}{\partial x} \right)_u + \left(\frac{\partial \phi_b}{\partial x} \right)_u, \tag{2.20}$$

$$V_l = U \cos \alpha + \dot{h} \sin \alpha + \left(\frac{\partial \phi_{lev}}{\partial x} \right)_l + \left(\frac{\partial \phi_{tev}}{\partial x} \right)_l + \left(\frac{\partial \phi_b}{\partial x} \right)_l. \tag{2.21}$$

Drawing from thin-aerofoil theory,

$$\left(\frac{\partial \phi_b}{\partial x} \right)_u = \frac{\gamma(x)}{2}, \tag{2.22}$$

$$\left(\frac{\partial\phi_b}{\partial x}\right)_l = -\frac{\gamma(x)}{2}, \quad (2.23)$$

$$V_{t_u}^2 - V_{t_l}^2 = 2 \left(U \cos \alpha + \dot{h} \sin \alpha + \left(\frac{\partial\phi_{lev}}{\partial x}\right) + \left(\frac{\partial\phi_{tev}}{\partial x}\right) \right) \gamma(x), \quad (2.24)$$

$$\phi_u = \int_0^x \frac{\gamma(x)}{2} dx + \int_0^x \left(\frac{\partial\phi_{lev}}{\partial x}\right) dx + \int_0^x \left(\frac{\partial\phi_{tev}}{\partial x}\right) dx, \quad (2.25)$$

$$\phi_l = - \int_0^x \frac{\gamma(x)}{2} dx + \int_0^x \left(\frac{\partial\phi_{lev}}{\partial x}\right) dx + \int_0^x \left(\frac{\partial\phi_{tev}}{\partial x}\right) dx, \quad (2.26)$$

$$\left(\frac{\partial\phi}{\partial t}\right)_u - \left(\frac{\partial\phi}{\partial t}\right)_l = \frac{\partial}{\partial t} \int_0^x \gamma(x) dx. \quad (2.27)$$

From (2.18), (2.24) and (2.27),

$$\Delta p(x) = \rho \left[\left(U \cos \alpha + \dot{h} \sin \alpha + \left(\frac{\partial\phi_{lev}}{\partial x}\right) + \left(\frac{\partial\phi_{tev}}{\partial x}\right) \right) \gamma(x) + \frac{\partial}{\partial t} \int_0^x \gamma(x) dx \right]. \quad (2.28)$$

The normal force on the aerofoil is obtained by integrating the pressure coefficient over the chord,

$$F_N = \rho \left[\int_0^c \left(U \cos \alpha + \dot{h} \sin \alpha + \left(\frac{\partial\phi_{lev}}{\partial x}\right) + \left(\frac{\partial\phi_{tev}}{\partial x}\right) \right) \gamma(x, t) dx + \int_0^c \frac{\partial}{\partial t} \int_0^x \gamma(x_0, t) dx_0 dx \right]. \quad (2.29)$$

Evaluating using the Fourier coefficients gives

$$F_N = \rho \pi c U \left[\left(U \cos \alpha + \dot{h} \sin \alpha \right) \left(A_0(t) + \frac{1}{2} A_1(t) \right) + c \left(\frac{3}{4} \dot{A}_0(t) + \frac{1}{4} \dot{A}_1(t) + \frac{1}{8} \dot{A}_2(t) \right) \right] + \rho \int_0^c \left(\left(\frac{\partial\phi_{lev}}{\partial x}\right) + \left(\frac{\partial\phi_{tev}}{\partial x}\right) \right) \gamma(x, t) dx. \quad (2.30)$$

In addition to the normal force, there is a leading-edge suction force acting axial to the aerofoil, given by the Blasius formula (Katz & Plotkin 2000). Employing the current formulation gives

$$F_S = \rho \pi c U^2 A_0^2. \quad (2.31)$$

The moment on the aerofoil is

$$M = \int_0^c \Delta p(x_{ref} - x) dx = x_{ref} F_N - \rho \pi c^2 U \left[\left(U \cos \alpha + \dot{h} \sin \alpha \right) \left(\frac{1}{4} A_0(t) + \frac{1}{4} A_1(t) - \frac{1}{8} A_2(t) \right) + c \left(\frac{7}{16} \dot{A}_0(t) + \frac{11}{64} \dot{A}_1(t) + \frac{1}{16} \dot{A}_2(t) - \frac{1}{64} \dot{A}_3(t) \right) \right] - \rho \int_0^c \left(\left(\frac{\partial\phi_{lev}}{\partial x}\right) + \left(\frac{\partial\phi_{tev}}{\partial x}\right) \right) \gamma(x, t) x dx. \quad (2.32)$$

The force coefficients (C_N and C_S) are evaluated by dividing the forces with $(1/2)\rho U^2 c$ and the moment coefficient (C_m) is obtained as $M/(1/2)\rho U^2 c^2$. The lift and drag coefficients on the aerofoil are:

$$C_l = C_N \cos \alpha + C_S \sin \alpha, \quad (2.33)$$

$$C_d = C_N \sin \alpha - C_S \cos \alpha. \quad (2.34)$$

2.5. Summary of the LESP-modulated discrete-vortex method

The LDVM presented in this paper is a time-stepping scheme in which the bound vorticity on the aerofoil is represented as a Fourier series. At each time step, one discrete vortex is shed from the aerofoil trailing edge. A Newton–Raphson iteration is used to determine the strength of the shed vortex such that the flow is tangential to the aerofoil surface and Kelvin’s circulation theorem is enforced. Then, the instantaneous LESP value, $A_0(t)$, is compared to the critical LESP value. If the absolute value of LESP(t) is greater than the critical LESP value, an LEV is shed. In this case, the strengths of the LEV and TEV are determined using a two-dimensional Newton–Raphson iteration such that flow is tangential to the aerofoil surface, Kelvin’s circulation theorem is enforced and $LESP(t) = LESP_{crit}$. The forces and moments on the aerofoil are then calculated. Finally, all the free vortices in the flow field are convected with the induced velocities (due to all other free and bound vortices) acting at their centres and the simulation moves on to the next time step. This procedure is presented as a flow chart in figure 5.

3. Validation and results

The LDVM is validated against experimental and computational data generated by the present authors and against data from recent literature. Five case studies are used to test the method for various aerofoil shapes, Reynolds numbers, and motion types. For each case study, the single value of critical LESP is obtained empirically. This value depends on the aerofoil and the operating Reynolds number but is independent of motion kinematics. For case studies 1, 2, and 3, the values of critical LESP were obtained using our CFD code (REACTMB-INS) for a calibration 0° – 90° pitch motion, as described in appendix A. For case studies 4 and 5, which use data from literature (Kinsey & Dumas 2008; Wang & Eldredge 2013), the critical LESP value for each case was determined as that value which minimised the difference between the loads predicted by the LDVM and the data provided in the respective papers.

The five case studies were specifically selected to (i) test the method in a challenging motion kinematic in which the LEV has strong interaction with the aerofoil wall flow (case study 1), (ii) evaluate the effectiveness of the method for a motion involving high motion amplitude and rate, and intermittent LEV formation on upper and lower surfaces (case study 2), (iii) evaluate the effectiveness of the method for different types of LEV shedding and highlight conditions under which the method fails to correctly predict loads owing to the occurrence of trailing-edge separation without LEV formation (case study 3), (iv) highlight the importance of the LESP criterion by comparing results for sinusoidal motions with and without the LESP-based shedding criterion (case study 4), and (v) study the results from the method for a flat-plate geometry at a high pitch angle when alternating vortex shedding occurs (case study 5).

Descriptions of the relevant motion kinematics are provided in each subsection. Details of the motion parameters along with critical LESP values and run-times of the LDVM code for each case are listed in appendix B. Case studies 1, 2, and 3

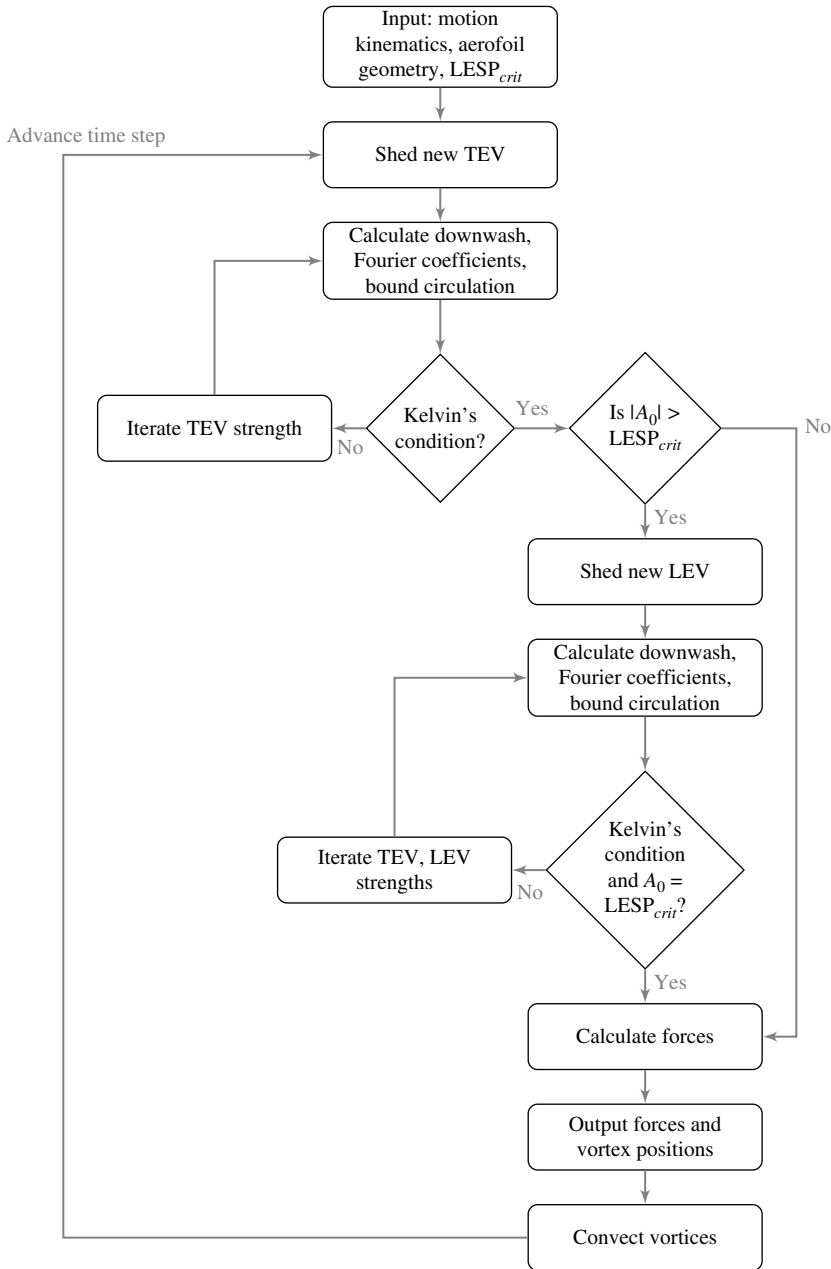


FIGURE 5. Flow chart depicting summary of the LDVM.

use the SD7003 aerofoil. The different critical-LESP values for these cases is a consequence of the different Reynolds numbers used in these cases.

3.1. Case study 1: SD7003 aerofoil at $Re = 30\,000$

In this case study, the force and flow-field results from the LDVM are compared to experimental and computational data generated by the present authors. An SD7003

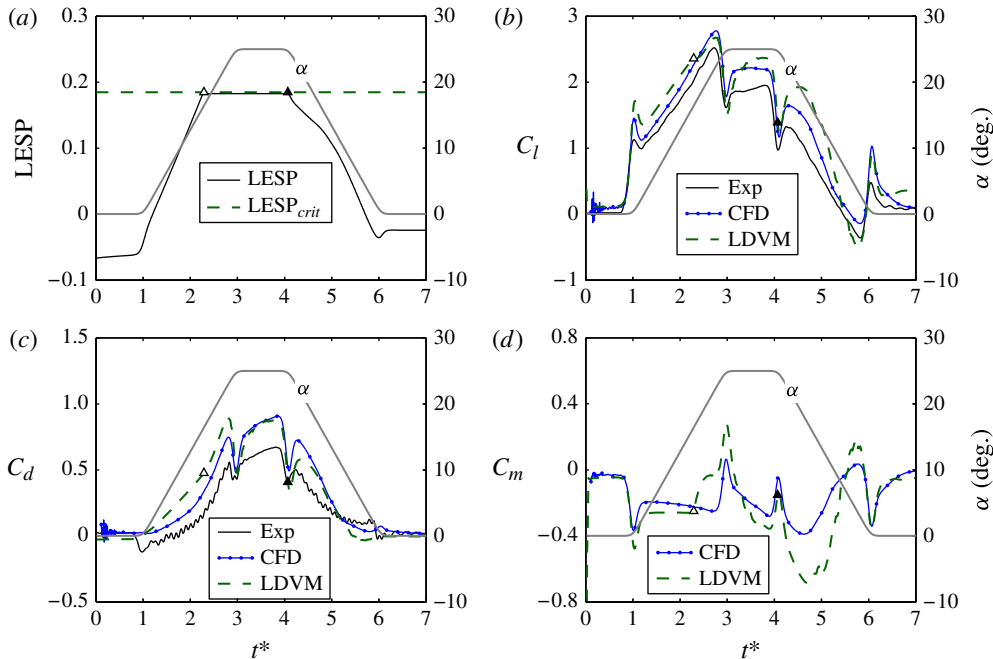


FIGURE 6. (Colour online) Case study 1 (SD7003, $Re = 30\,000$): LESP and loads. Variation with $t^* = tU/c$ of: (a) LESP from LDVM, (b) lift coefficient from LDVM, CFD and experiment, (c) drag coefficient from LDVM, CFD and experiment, (d) pitching-moment coefficient about the quarter-chord from LDVM and CFD. The initiation and termination of LEV shedding is marked on the LDVM curves using open and filled triangles respectively, with upper- and lower-facing triangles indicating upper- and lower-surface LEV shedding. The right-hand axes show the scale for pitch-angle variation, $\alpha(t^*)$ shown as the grey curve.

aerofoil (Selig, Donovan & Fraser 1989) at a Reynolds number of 30 000 is used for this test case. The pitch–hold–return motion with sharp corners used here is generated using the Eldredge function (Eldredge *et al.* 2009) with a smoothing parameter $a = 11$. The amplitude of pitch is 25° , pivot is at the leading edge, and the non-dimensional pitch rate, K , is 0.11. The variation of pitch angle with non-dimensional time, $t^* = tU/c$, is plotted in figure 6. The critical LESP was pre-determined from CFD using the approach described in appendix A to be 0.18.

The experiments were performed at the US Air Force Research Laboratory’s (AFRL) Horizontal Free-surface Water Tunnel, which is fitted with a three degree of freedom electric motion rig enabling independent control of pitch, plunge and surge (streamwise-aligned translation). More detail on the rig operation is given in Ol *et al.* (2009a) and Granlund, Ol & Bernal (2011), while the facility is discussed in Ol *et al.* (2005). The flow field is visualized by planar laser fluorescence. A high concentration of Rhodamine 6G in water is injected at the leading and trailing edges at 3/4-span locations by a positive-displacement pump at a prescribed volumetric infusion rate, via a 0.5 mm diameter internal rigid line, as documented by Ol *et al.* (2009a). The dye is illuminated by an Nd:YLF 527 nm pulsed laser sheet of 1.5 mm thickness at 50 Hz and images are recorded with a PCO DiMax high-speed camera through a Nikon PC-E 45 mm Micro lens. An orange Wratten no. 21 filter removes the incident

and reflected laser light since the dye fluorescence wavelength is 566 nm. Force data are recorded from an ATI Nano-25 IP68 six-component integral loadcell, oriented with its cylindrical axis normal to the pitch–plunge–surge plane. Experimental force data are ensemble averaged over ten repetitions of the motion.

The CFD calculations were performed using NCSU's REACTMB-INS code, which solves the time-dependent incompressible Navier–Stokes equations using a finite-volume method. The governing equations are written in arbitrary Lagrangian/Eulerian (ALE) form, which enables the motion of a body-fitted computational mesh in accord with prescribed rate laws. An implicit, dual-time-stepping artificial compressibility method is used for time advancement, with sub-iterations performed at each physical time step to adjust the flow to the new position of the body and to converge the continuity equation. Spatial discretisation of the inviscid fluxes uses a low-diffusion flux-splitting method valid in the incompressible limit (Cassidy, Edwards & Tian 2009). The Spalart–Allmaras model (Spalart & Allmaras 1992) as implemented by Edwards & Chandra (1996), is used for turbulence closure. The cases studied, however, are at low Reynolds numbers and turbulence-model effects are generally confined to the wake. The computations were performed on a two-dimensional body-fitted mesh containing 92 400 cells. REACTMB-INS has been used for a wide variety of CFD problems, including unsteady aerodynamics (Ol *et al.* 2009*b*; Ramesh *et al.* 2013*b*), two-phase flows (Cassidy *et al.* 2009), human-induced contaminant transport (Choi & Edwards 2008, 2012), and moving-body flows (Choi *et al.* 2007).

Figure 6(*a*) shows the variation of LESP from the LDVM. The critical value of LESP of 0.18 is marked as a dashed line. We see that the LESP increases with pitch angle during the pitch-up motion until it reaches the critical value at approximately $t^* = 2$. This time instant corresponds to the initiation of LEV formation. The critical value of LESP governs the maximum suction that can be supported by the leading edge at this Reynolds number. Based on this assumption, LESP is maintained at the critical value through discrete-vortex shedding of appropriate strength (at each time step) as long as the motion/flow conditions are such that LESP would otherwise exceed the critical value. The clockwise discrete vortices shed in this case form an upper-surface LEV. Towards the end of the hold, the LESP falls below the critical value resulting in termination of upper-surface LEV shedding. Even though the pitch angle is high at this time in the motion, this decrease in LESP is a consequence of the downwash at the leading edge induced by the vortices shed from the leading and trailing edges. Thus, with the use of a single empirically-obtained parameter (the critical value for LESP), the LESP concept governs the initiation, growth and termination of LEV formation.

Figure 6(*b,c*) compares the lift-coefficient and drag-coefficient variations with t^* from LDVM, CFD, and experiment. First, comparing CFD and experiment, we see that C_l from experiment is lower than that from CFD during the hold and downstroke, i.e. from t^* of 3 to 6; C_d from experiment is lower than that from CFD for most of the motion. Second, we note that the LDVM correctly captures the locations and the intensities of the spikes in the C_l and C_d time histories. These spikes are due to apparent-mass effects. From the start of the motion until the end of the hold, i.e. from $t^* = 0$ to 4, C_l from the LDVM matches reasonably well with CFD predictions. During the downstroke, the LDVM over-predicts C_l compared to CFD by approximately the same amount by which experiment under-predicts CFD. Figure 6(*d*) compares the pitching moment coefficient about the quarter-chord location, C_m , from the LDVM with CFD predictions. Pitching moment measurements are not available from experiment. It is seen that C_m from the LDVM compares reasonably well with

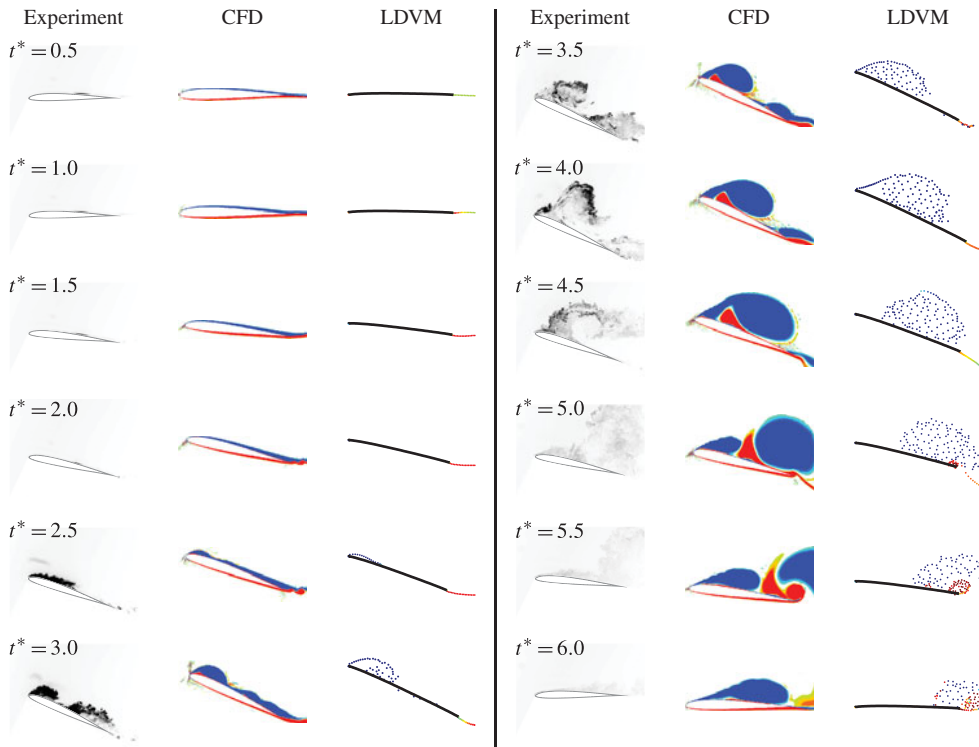


FIGURE 7. (Colour online) Case study 1 (SD7003, $Re = 30\,000$): flow features. Comparison of flow features between LDVM, CFD and experiment for t^* from 0.5 to 6.0. To each dye-flow image, the aerofoil contour has been added to provide context.

CFD except in the downstroke region, where C_m from the LDVM is noticeably more negative than the CFD prediction.

In figure 7, dye flow images from experiment, vorticity contours from CFD and point-vortex plots from the LDVM are compared at equally spaced time intervals. The LDVM prediction of LEV initiation at shortly after $t^* = 2$ is corroborated by the accumulation at the leading edge of dye in experiment and vorticity in CFD at $t^* = 2.5$. The growth and chordwise location of the LEV during $t^* = 2.5$ – 4.0 are qualitatively in agreement between the three methods. While LDVM and experiment predict a termination of LEV formation shortly after $t^* = 4$, CFD predicts the termination only after $t^* = 4.5$. Between $t^* = 3.5$ and 5.0 , CFD shows two flow features that are not modelled in the LDVM: (i) a buildup of counter-clockwise vorticity below the LEV and adjacent to the upper surface during $t^* = 3.5$ to 4.5 and (ii) a concentration of clockwise vorticity near the leading edge at $t^* = 5.0$ that is subsequently convected downstream along the chord. These two flow features appear to be related, with the growth in counter-clockwise vorticity apparently cutting off and causing detachment of the feeding sheet for the LEV shortly after $t^* = 4.5$, resulting in the concentration of clockwise vorticity near the leading edge at $t^* = 5.0$. Another CFD-predicted flow feature that is not captured in the LDVM prediction is the trailing-edge separation between $t^* = 2.5$ and 4.0 . The phenomena causing these features are not modelled in the LDVM. In this challenging case study in which the strong LEV is convected close to the upper surface over the chord causing strong interactions between the LEV and

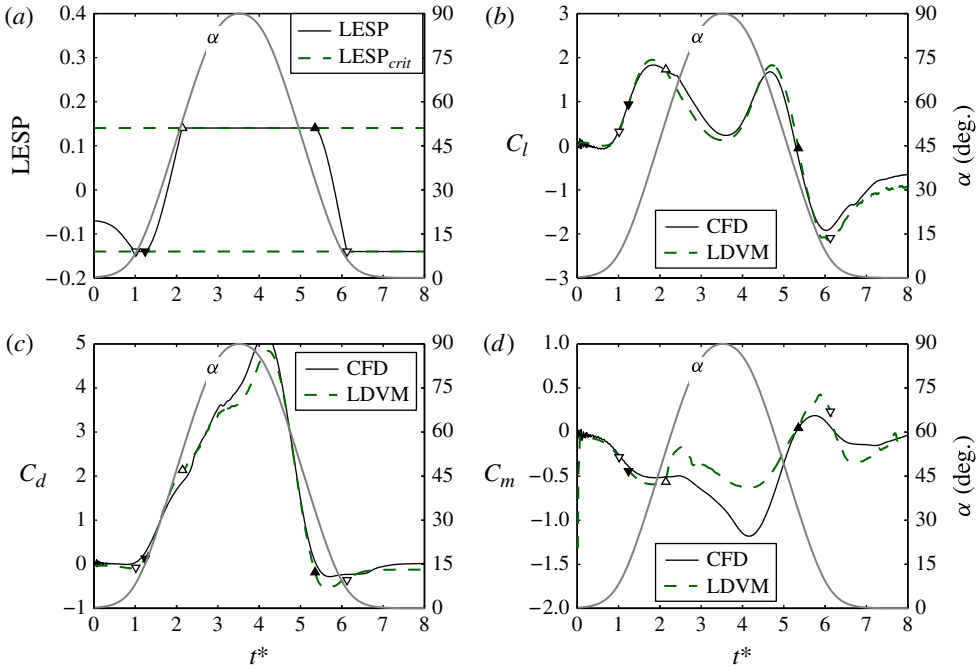


FIGURE 8. (Colour online) Case study 2 (SD7003, $Re = 100\,000$): LESP and loads. Variation with $t^* = tU/c$ of: (a) LESP from LDVM, (b) lift coefficient from LDVM and CFD, (c) drag coefficient from LDVM and CFD, (d) pitching-moment coefficient about the quarter-chord from LDVM and CFD. The initiation and termination of LEV shedding is marked on the LDVM curves using open and filled triangles respectively, with upper- and lower-facing triangles indicating upper- and lower-surface LEV shedding. The right-hand axes show the scale for pitch-angle variation, $\alpha(t^*)$.

the upper-surface wall flow, the absence of these flow features in the LDVM is likely to be the reason for the discrepancies in the force predictions seen in figure 6(b–d).

3.2. Case study 2: SD7003 aerofoil at $Re = 100\,000$

In this case study, an SD7003 aerofoil undergoing a smoothed pitch-up–return motion is considered. In comparison with case study 1, the motion in this case study involves a higher pitch rate of $K = 0.4$, larger pitch amplitude of 90° , and larger Reynolds number of $100\,000$. Since this motion is beyond the capabilities of our experimental facility, the LDVM is compared only with CFD results from our REACTMB-INS code. The SD7003 aerofoil pivoting about the trailing edge is pitched up from 0° to 90° and brought back to 0° using a half-sine-like function generated with the Eldredge function and smoothing parameter $a = 2$. The pitch variation with t^* is shown in figure 8(a–d). The critical LESP for this aerofoil and Reynolds number was predetermined from CFD, using the approach described in appendix A, to be 0.14.

Figure 8(a) shows the time variation of LESP for this case, with the positive and negative values of the critical LESP marked as dashed lines. Figure 8(b–d) compares the variations of lift, drag, and moment coefficients from LDVM and CFD. The flow predictions from LDVM are compared with CFD results at equally spaced times in figure 9.

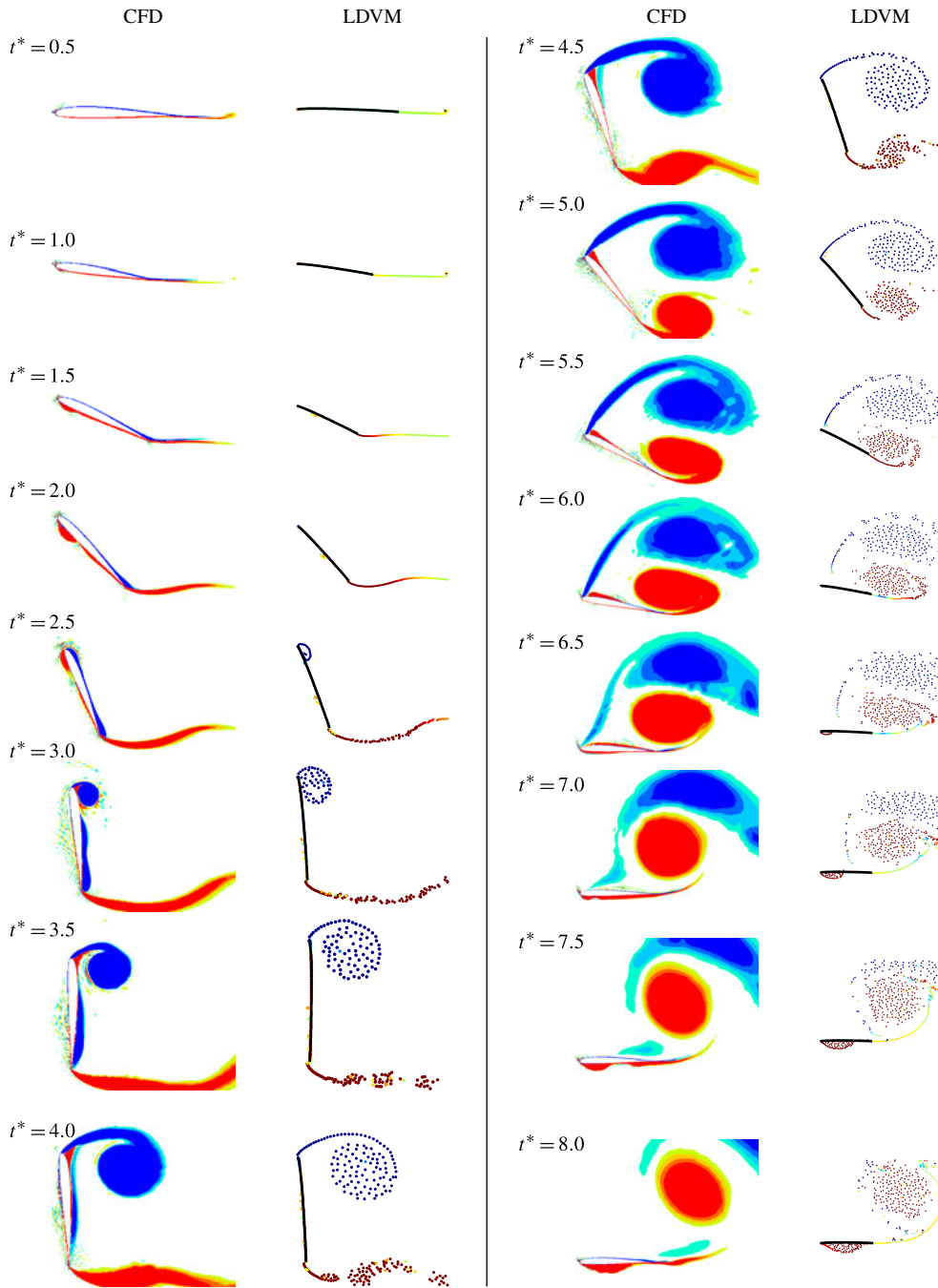


FIGURE 9. (Colour online) Case study 2 (SD7003, $Re = 100\,000$): flow features. Comparison of flow features between the LDVM and CFD for t^* from 0.5 to 8.0.

Examining the LESP variation in figure 8(a) first, we see that the LESP decreases at the start of the motion until it reaches the negative LESP critical value. This decrease in LESP occurs even though the aerofoil is pitching to higher angles because the pivot point is at the trailing edge. Pitch rate about the trailing edge causes a motion-induced downwash at the leading edge, which is manifested as a decreasing LESP at the initial times. With increasing pitch angle, the effect of the motion-induced downwash is soon overcome, and the LESP rapidly increases shortly after t^* of 1.0. Because the decreasing LESP reaches the negative critical value of -0.14 , the LDVM keeps the LESP constrained to this limit by shedding counter-clockwise discrete vortices at every time step until the increase in LESP results in LESP becoming higher than the negative critical value. The resulting small LEV is seen being convected along the lower surface of the aerofoil in both LDVM and CFD flow pictures in figure 9 at $t^* = 1.5$ and 2.0. The rapidly increasing LESP then reaches the positive critical LESP of $+0.14$ shortly after $t^* = 2$ and is maintained at this critical value by shedding of clockwise discrete vortices at every time step until t^* is approximately 5.5. The formation, growth, and termination of the resulting large LEV is clearly seen in both the LDVM and CFD flow snapshots in figure 9 during t^* from 2.5 to 6.0. The LDVM prediction of the growth of this large LEV and its interaction with the counter-clockwise TEV compare well with the CFD prediction. Shortly after $t^* = 6.0$, when the aerofoil is at a low pitch angle during the downstroke, the large counter-clockwise TEV that is close to the aerofoil induces a downwash at the leading edge. This causes the LESP to rapidly decrease and reach the negative critical LESP value, resulting in shedding of counter-clockwise discrete vortices from the leading edge, which forms an LEV on the aerofoil lower surface until the end of the motion at $t^* = 8$. This LEV on the lower surface is also seen in the CFD result in figure 9.

Examining figure 8(b–d), we see that the predictions of lift and drag coefficients from the LDVM are in excellent agreement with the CFD predictions. While the LDVM results for C_m are close to those from CFD, there is some discrepancy between t^* of 2.0 and 7.0. This discrepancy could be a result of the thick boundary layers on the aerofoil surfaces seen in CFD, which are not accounted for in the LDVM. Overall, the LDVM is seen to perform remarkably well in predicting the force coefficients and the flow, even when there is intermittent LEV formation on alternating surfaces.

3.3. Case study 3: sinusoidal pitch–plunge SD7003 aerofoil at $Re = 10\,000$

In this case study, we consider three pitch–plunge motions of the SD7003 aerofoil at a Reynolds number of 10 000. These cases are taken from the pitch–plunge equivalence study of McGowan *et al.* (2011), in which several such motions were studied to evaluate the effectiveness of Theodorsen’s theory at high reduced frequencies and non-dimensional amplitudes. The three cases selected for this case study were chosen to evaluate the effectiveness of the LDVM in predicting flow and lift behaviour in the presence of different types of LEV shedding. We compare flow and lift predictions from the LDVM with results from Theodorsen’s theory, CFD results from the CFL3D code (Krist, Biedron & Rumsey 1998), and experiments from the AFRL water-tunnel facility. The CFD and experimental results are taken from McGowan *et al.* (2011).

In case 3A, a pitch–plunge combination is studied at a high reduced frequency of $k = 3.93$, which results in a ratio of convective time, $t_c = c/U$, to time period, T , of $t_c/T = 1.25$. In this case, the clockwise and counter-clockwise LEVs that are shed

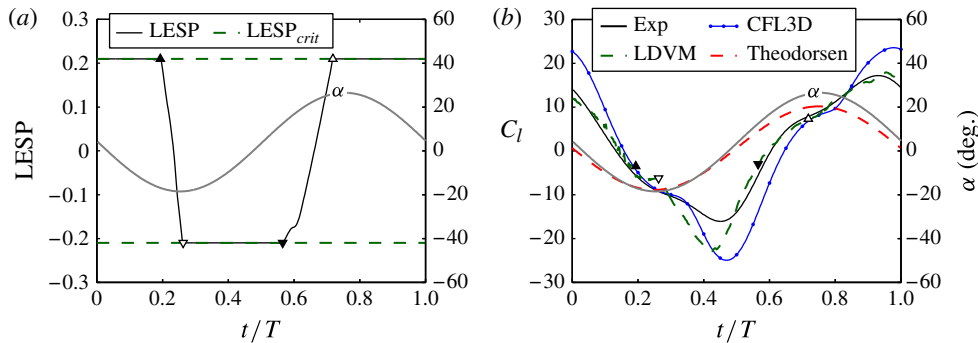


FIGURE 10. (Colour online) Case study 3A (SD7003, $Re = 10000$): LESP and loads. Variation with t/T of: (a) LESP from LDVM, (b) lift coefficient from Theodorsen, LDVM, CFD and experiment. The initiation and termination of LEV shedding is marked on the LDVM curves using open and filled triangles respectively, with upper- and lower-facing triangles indicating upper- and lower-surface LEV shedding. The right-hand axes show the scale for pitch-angle variation, $\alpha(t^*)$.

during a time cycle remain close to the leading edge and result in strong interactions between each other, leading to strong effects of the vortices on the lift. As a result, Theodorsen's theory fails to predict the lift variation correctly for this case. In cases 3B and 3C, the reduced frequency of $k = 0.393$ is a tenth of that used in 3A, and the convective time, $t_c = c/U$, is about one eighth of the time period, T . In case 3B, the upper- and lower-surface LEVs that form during a cycle are deformed and convected downstream well before a cycle is complete. In case 3C, no LEVs are formed, but there is significant trailing-edge separation. The motion parameters for these three cases are listed in appendix B. The critical LESP value of 0.21 for this case study was obtained using the method outlined in appendix A, and is used for the three cases 3A, 3B, and 3C.

We start with case 3A. Figure 10(a) shows the time variation of LESP along with the critical LESP values marked as dashed lines. We see that, at the start of the cycle, LESP is at the positive critical-LESP value until approximately t/T of 0.2. Shortly after the termination of the resulting upper-surface LEV, the LESP drops rapidly to reach the negative critical-LESP value and stays there for approximately a third of the cycle. During this time, counter-clockwise discrete vortices are shed, which form a lower-surface LEV. Because of the high k , the resulting LEVs are not convected downstream rapidly, and end up staying close to the leading edge for a considerable portion of the cycle. Figure 11 compares the flow visualisation for two times instants in a cycle from experiments using dye flow, CFD using vorticity plots and the LDVM using discrete vortices. It is seen that predictions for the LEV formation, as visualised in the three methods, are in good agreement with each other. There is an upper-surface LEV being formed at $t/T = 0$, and a lower-surface LEV at $t/T = 0.5$. Also seen is that when the LEV is being formed on one surface, the earlier LEV from the other surface (from approximately half a cycle earlier) is still in the vicinity of the leading edge, resulting in complex vortex interaction. Figure 10(b) compares the time variation of the lift coefficient from Theodorsen's theory, experiment, CFD, and the LDVM. Although Theodorsen's theory takes into consideration the unsteady effects due to apparent mass and trailing-wake vorticity, it assumes an attached flow at the leading edge. In this case, that assumption is severely violated. As a result, the prediction

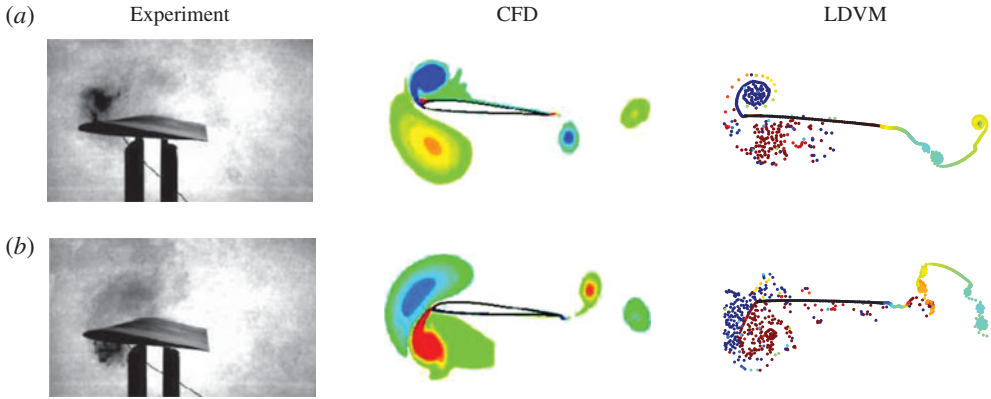


FIGURE 11. (Colour online) Case study 3A (SD7003, $Re = 10\,000$): flow features. Comparison of flow features between LDVM, CFD and experiment at two time instants: (a) $t/T = 0$ and (b) $t/T = 0.5$.

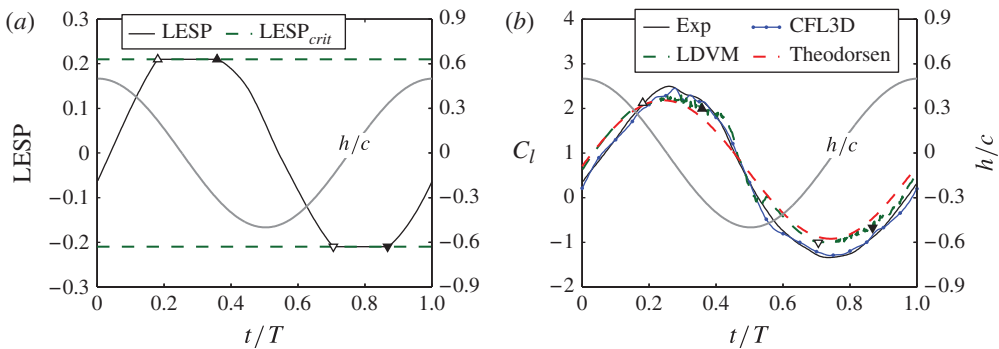


FIGURE 12. (Colour online) Case study 3B (SD7003, $Re = 10\,000$): LESP and loads. Variation with t/T of: (a) LESP from LDVM, (b) lift coefficient from Theodorsen, LDVM, CFD and experiment. The initiation and termination of LEV shedding is marked on the LDVM curves using open and filled triangles respectively, with upper- and lower-facing triangles indicating upper- and lower-surface LEV shedding. The right-hand axes show variation in plunge for this case, since there is no variation in pitch.

from Theodorsen's theory is not in agreement with those from experiment and CFD. Experiment, CFD, and LDVM are seen to predict lift variations that are broadly in agreement with each other.

We now move to the discussion of case 3B. The variation of LESP is compared with the positive and negative critical-LESP values in figure 12(a). The LESP is at the positive critical value from t/T shortly before 0.2 to approximately 0.4, during which time clockwise discrete vortices are shed from the leading edge, which form an upper-surface LEV. This LEV is deformed and convected downstream during the formation because of the small t_c/T ratio. During t/T from approximately 0.7 to 0.9, an LEV is formed on the lower surface. The flow visualisation from experiment, CFD, and the LDVM, shown in figure 13 for t/T of 0 and 0.5, generally confirm the conclusions drawn from the LESP variation. The flow visualisations from the three

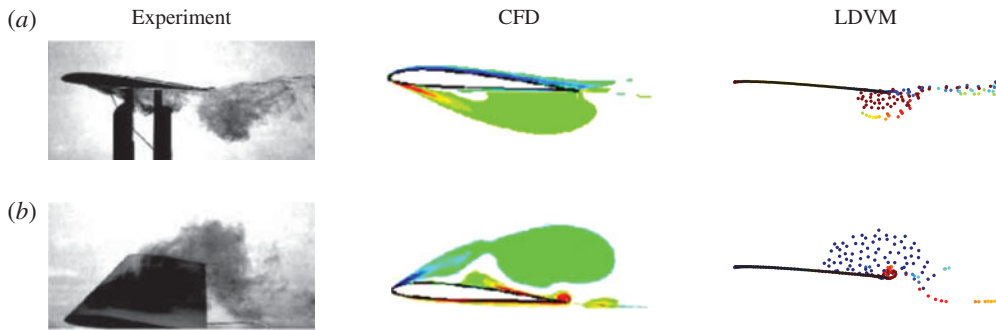


FIGURE 13. (Colour online) Case study 3B (SD7003, $Re = 10k$): flow features. Comparison of flow features between LDVM, CFD and experiment at two time instants: (a) $t/T = 0$ and (b) $t/T = 0.5$.

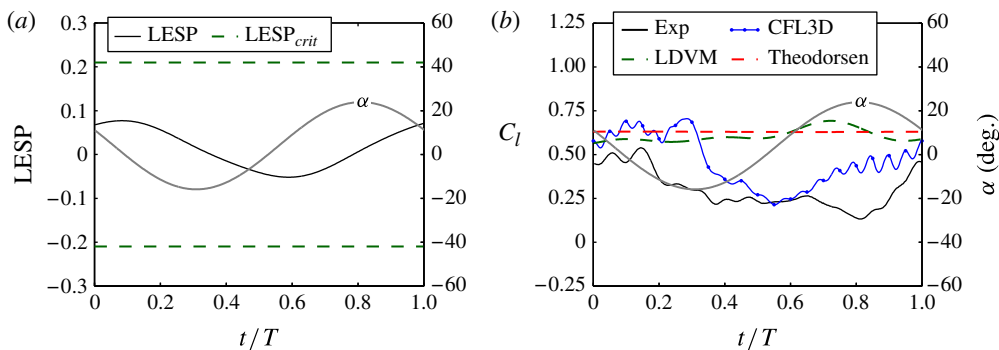


FIGURE 14. (Colour online) Case study 3C (SD7003, $Re = 10000$): LESP and loads. Variation with t/T of: (a) LESP from LDVM, (b) lift coefficient from Theodorsen, LDVM, CFD and experiment. The right-hand axes show the scale for pitch-angle variation, $\alpha(t^*)$.

methods are in general agreement with each other although a ‘feeding sheet’ from the leading edge to the LEV is visible in the experiment and CFD, but not in the LDVM. The lift-coefficient variations from Theodorsen’s theory, experiment, CFD, and LDVM in figure 12(b) are seen to be in good agreement with each other.

The final case in this section, case 3C, is one which should have no time variation in the lift coefficient from Theodorsen’s theory due to perfect cancellation of the circulatory and non-circulatory contributions at all times. From Theodorsen’s theory, this motion has a constant lift coefficient which arises from the mean pitch angle of 4° and the aerofoil zero-lift angle of attack to which the sinusoidal pitch variation is added. The LESP variation, shown in figure 14(a), does not reach either the positive or negative LESP-critical value at any point during the cycle. The LDVM, therefore, predicts that there should be no LEV generated with this motion. That prediction is clearly corroborated by the flow visualisation from experiment, CFD, and LDVM in figure 15. As seen from the experiment and CFD flow visualisations for $t/T = 0.5$, there is significant amount of boundary-layer separation over the aft half of the upper surface, which is not modelled in the LDVM. Figure 14(b) shows the time variation of the lift coefficient from Theodorsen’s theory, experiment, CFD,

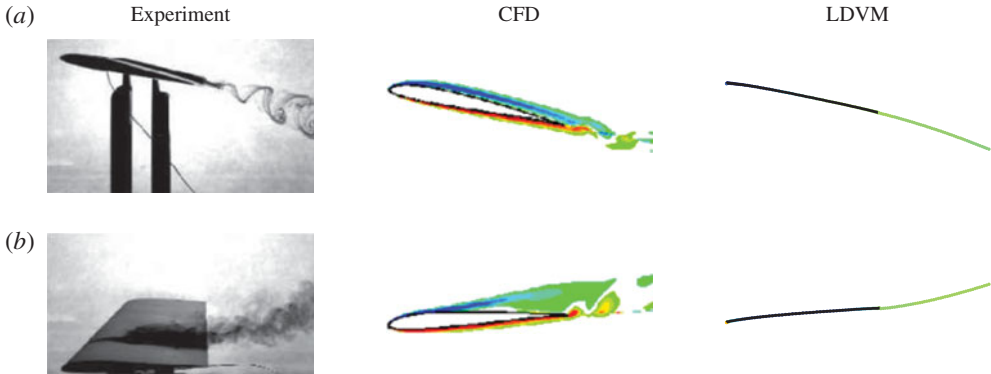


FIGURE 15. (Colour online) Case study 3C (SD7003, $Re = 10\,000$): flow features. Comparison of flow features between LDVM, CFD and experiment at two time instants: (a) $t/T = 0$ and (b) $t/T = 0.5$.

and LDVM. Theodorsen's theory predicts a uniform lift coefficient of approximately 0.63. The predicted lift-coefficient variation from LDVM largely agrees with that from Theodorsen's method. Small disagreements are attributed to the removal of small-angle and flat-wake approximations in the LDVM formulation. Lift-coefficient variations from Theodorsen's method and LDVM do not match well with those from experiment and CFD. The discrepancy is because Theodorsen's method and LDVM do not model the boundary-layer separation over the aft portion of the aerofoil.

3.4. Case study 4: sinusoidal pitch–plunge with NACA 0015 at $Re = 1100$

In this case study, we consider sinusoidal pitch–plunge motions of an NACA 0015 aerofoil from Kinsey & Dumas (2008), who evaluated the aerofoil undergoing oscillating motions for power extraction from a moving fluid at a Reynolds number of 1100. We validate the LDVM by comparison with CFD data published by Kinsey & Dumas (2008). As shown in recent studies (Kinsey & Dumas 2008; Zhu 2011; Bryant, Gomez & Garcia 2013; Young *et al.* 2013; Young, Lai & Platzer 2014), such oscillatory motions result in periodic LEV formation and shedding, making them good candidates for validation of the current LDVM. In the current case study, we examine one pitch–plunge motion for which detailed results are presented in Kinsey & Dumas (2008) from CFD calculations using the FLUENT code, assuming laminar flow. Because we do not have access to skin-friction information from the CFD results in Kinsey & Dumas (2008), it is not possible to use the method of appendix A to determine the critical LESP. Instead, we present another approach to empirically determine the critical LESP using time variations of force data in the literature. We used the LDVM to study the motion with various values of the critical LESP in an effort to determine which critical-LESP value would provide the best match in time variations of force coefficients with the available CFD force data from Kinsey & Dumas (2008). This approach was then used to select the critical LESP of 0.19 which was used for all other motions with this aerofoil at this Reynolds number.

The baseline motion in this case study has a sinusoidal oscillation in pitch angle with amplitude of 76.33° and frequency $f = 0.14$ combined with a sinusoidal plunge oscillation with the same frequency, amplitude of $h/c_{max} = 1$, with plunge leading pitch

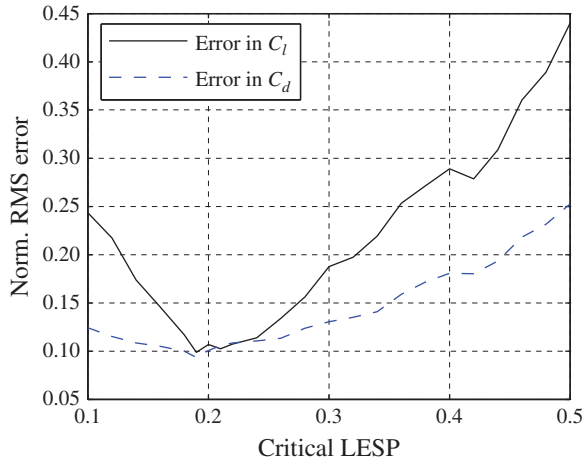


FIGURE 16. (Colour online) Case study 4 (NACA 0015, $Re = 1100$): normalised RMS errors in the lift and drag coefficients between the predictions from the LDVM and CFD, over a range of critical-LESP values.

by 90° . The pivot location for pitch is at the $c/3$ location for the baseline motion, although the effect of other pivot locations is examined later in this case study. For the baseline motion, we also present the sensitivity of lift, drag, and moment predictions to the choice of the critical-LESP value.

Figure 16 shows the effect of the critical LES on the normalised root-mean-square (RMS) error in lift and drag coefficients between CFD and LDVM predictions. The range of the lift and drag coefficient curves from CFD (maximum value minus minimum value) is used as the normalising factor for RMS errors in lift and drag respectively. The expression for normalised RMS error, shown here for the lift coefficient, is:

$$\text{Norm. RMS error}|_{C_l} = \frac{\sqrt{(C_{l_{LDVM}} - C_{l_{CFD}})^2}}{C_{l_{CFD,max}} - C_{l_{CFD,min}}}. \quad (3.1)$$

It is seen that both errors, each of which was determined independently of the other, have a clear minimum for a critical-LESP value of 0.19. The fact that both lift and drag errors are minimised for the same critical-LESP value lends further credence to the idea of a limiting value of the leading-edge suction and bolsters the argument that the LES is a single crucial theoretical parameter that governs the flow physics of aerofoils undergoing unsteady motions with LEV formation. From the results shown in figure 16, the critical LES for this case study was taken to be 0.19.

Figure 17(a) shows the time variation of LES for the baseline case, with the positive and negative values of the critical LES of 0.19 marked as dashed lines. It is seen that the LES starts to decrease at the beginning of the cycle, reaching and staying at the negative critical value for approximately a quarter of the cycle. With increasing pitch angle, the LES increases and reaches the positive critical value in the second half of the cycle, staying at that value again for approximately a quarter of the cycle. During the time when the LES is at the positive/negative critical value, clockwise/counter-clockwise discrete vortices are generated, which form an LEV that is shed from the upper/lower surface. Figure 17(b–d) compares the variations of lift,

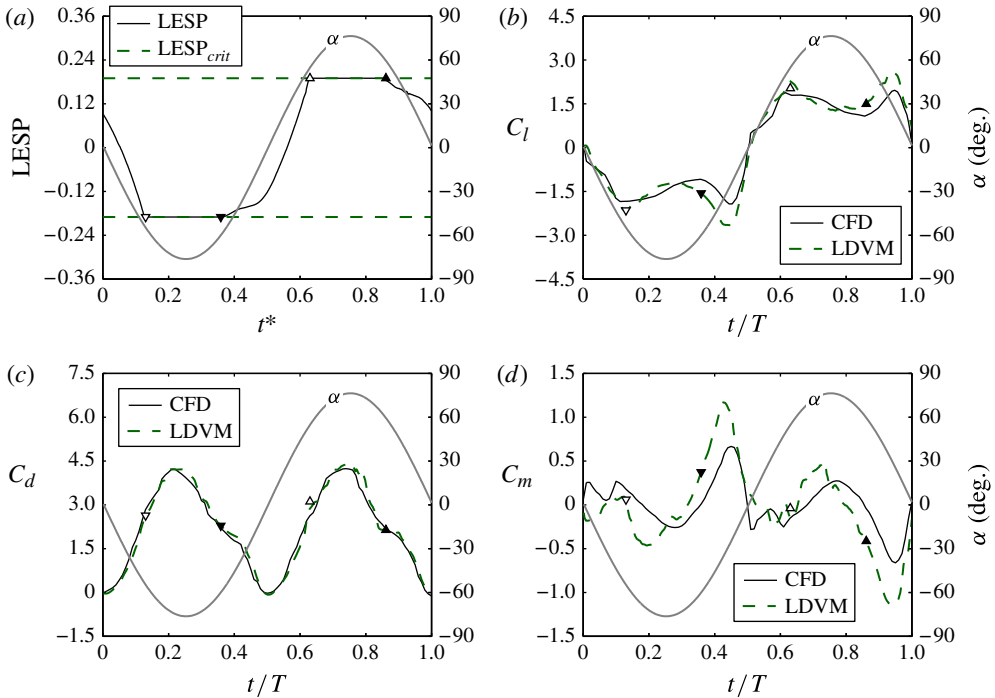


FIGURE 17. (Colour online) Case study 4 (NACA 0015, $Re = 1100$): LESP and loads. Variation with t/T of: (a) LESP from LDVM, (b) lift coefficient from LDVM and CFD, (c) drag coefficient from LDVM and CFD, (d) pitching-moment coefficient about one-third chord from LDVM and CFD. The CFD solutions are from Kinsey & Dumas (2008). The initiation and termination of LEV shedding is marked on the LDVM curves using open and filled triangles respectively, with upward/downward-pointing triangles indicating upper/lower-surface LEV shedding. The right-hand axes show the scale for pitch-angle variation, $\alpha(t^*)$.

drag, and moment coefficients from the LESP-modulated LDVM and CFD results in Kinsey & Dumas (2008). The comparison in lift is seen to be very good, with the LDVM capturing all of the trends that are seen in the CFD prediction. The comparison in drag is excellent. As with the other cases, pitching-moment prediction from the LDVM is seen to have some discrepancies compared to the CFD result, but the general behaviour is similar between the two methods.

To evaluate the effect of choice of the critical-LESP value, we study the lift, drag and moment variations for the baseline motion with three values of critical LESP: (i) the value of 0.19 obtained empirically, (ii) a very high value of 5, which will result in no LEV shedding, and (iii) a value of zero, which will result in LEV shedding at all times as if a Kutta condition were enforced at the leading edge. The results are plotted in figure 18 and compared with the CFD results from Kinsey & Dumas (2008).

The flow fields from the LDVM for $t/T = 0$ for the three critical-LESP values are compared with the CFD vorticity plot for the same time instant in figure 19. It is clearly seen that using the correct critical-LESP value results in the best match with the CFD results. For such flow simulations, modelling the flow without any LEV shedding, which is akin to using inviscid theoretical methods such as Theodorsen's, or modelling the flow with constant LEV shedding, which is correct only for a sharp

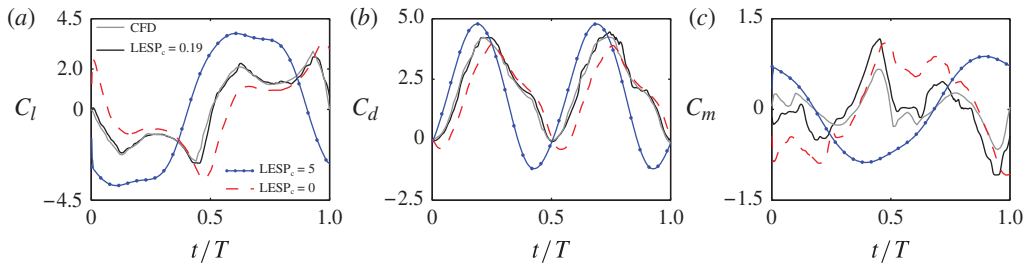


FIGURE 18. (Colour online) Case study 4 (NACA 0015, $Re = 1100$): effect of the critical LESP value: (a) lift, (b) drag and (c) moment-coefficient histories from the CFD results of Kinsey & Dumas (2008) and from the LDVM with: LEV shedding modulated by critical LESP of 0.19, no LEV shedding, owing to a very high critical LESP of 5.0, and LEV shedding at all times due to a critical LESP value of zero.

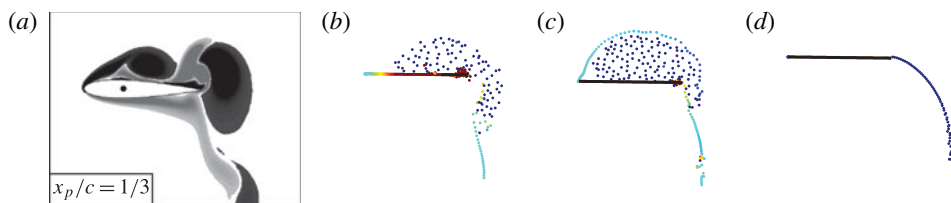


FIGURE 19. (Colour online) Case study 4 (NACA 0015, $Re = 1100$): flow field from LDVM at $t/T = 0$ for the three critical-LESP values, (b) 0.19, (c) 0 and (d) 5, compared with (a) the CFD vorticity plot for the same time instant.

leading edge, are both incorrect. The pitching-moment coefficient (where there are large differences between the three curves) especially illustrates the importance of regulated LEV shedding. Thus the LESP concept provides an excellent way to govern the formation, growth and termination of the LEV in such flows over aerofoils with rounded leading edges.

Figure 20(a) compares C_l predictions from the CFD results of Kinsey & Dumas (2008) for the baseline motion using three pivot locations: quarter-chord, one-third-chord, and half-chord. Figure 20(b) shows the same comparison from the LDVM. The same critical-LESP value of 0.19 is used for all these cases. Flow-field images from the LDVM are compared to vorticity plots from CFD results for the three pivot locations, at $t/T = 0$, in figure 21. The general trends due to pivot-location change are seen to be captured very well in the LDVM, further reinforcing the idea that the critical LESP is independent of the motion kinematics.

3.5. Case study 5: pitch-up manoeuvre with a flat plate at $Re = 1000$

In this case study, the flow over a 2.3%-thick flat-plate geometry with semi-circular leading and trailing edges at a Reynolds number of 1000 is studied. Two pitch-up ramp kinematics are considered in this section, both of which are of current interest to the AIAA Fluid Dynamics Technical Committee Low Reynolds Number Discussion Group. The LDVM is validated against results from UCLA's couplevpm code, a 2D viscous vortex particle method described in Eldredge (2007). We note that the flat-plate geometry used here does not have a sharp trailing edge, so that we cannot

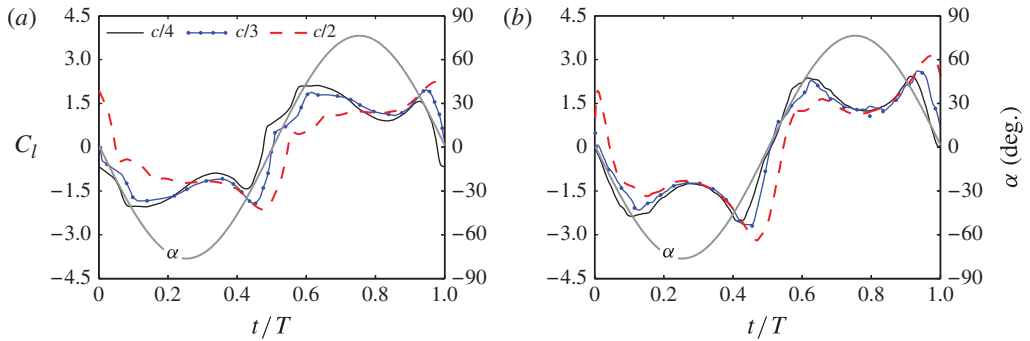


FIGURE 20. (Colour online) Case study 4 (NACA 0015, $Re = 1100$): effect of pivot location: lift-coefficient time histories for pivot locations of $c/4$, $c/3$, and $c/2$ from (a) CFD results of Kinsey & Dumas (2008) and (b) LDVM. The right-hand axes show the scale for pitch-angle variation, $\alpha(t^*)$.

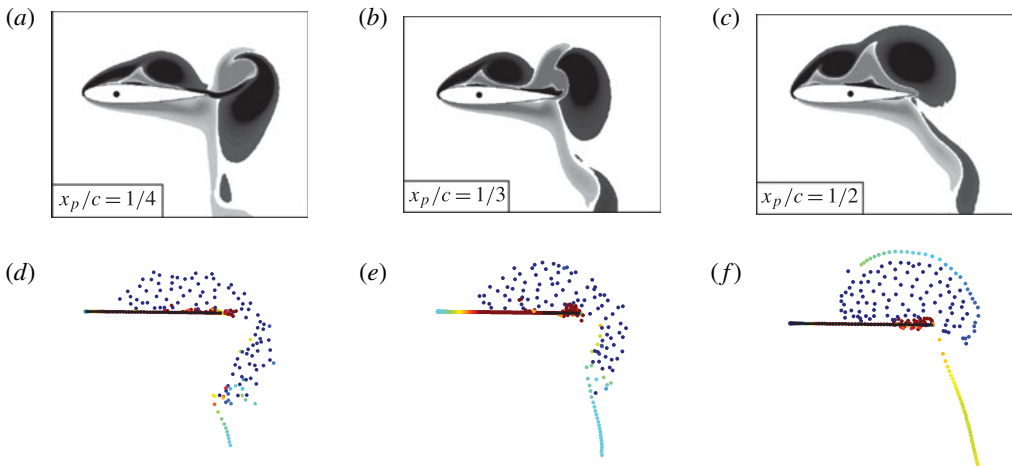


FIGURE 21. (Colour online) Case study 4 (NACA 0015, $Re = 1100$): flow-field from LDVM (*d-f*) at $t/T=0$ for the three pivot locations, compared with CFD vorticity plots reproduced with permission from Kinsey & Dumas (2008) (*a-c*) for the same cases.

expect the trailing-edge flow to satisfy the Kutta condition. Because our LDVM theory assumes that the trailing-edge Kutta condition is always satisfied, some discrepancy in the LDVM results is to be expected. As was done in case study 4, the critical value of LESP was determined using a minimisation approach to find the best match with lift and drag time variations available from CFD. The couplevpm prediction for the first motion (case 5A) was used as the reference data, and the critical LESP value was found to be 0.11. This value was then used for both motions (cases 5A and 5B).

The first pitch-ramp, studied in Wang & Eldredge (2013), is generated using an Eldredge function for a pitch up from 0° to 90° about the leading edge, with a non-dimensional pitch rate of $K = 0.2$ and smoothing parameter $a = 11$. The motion ends

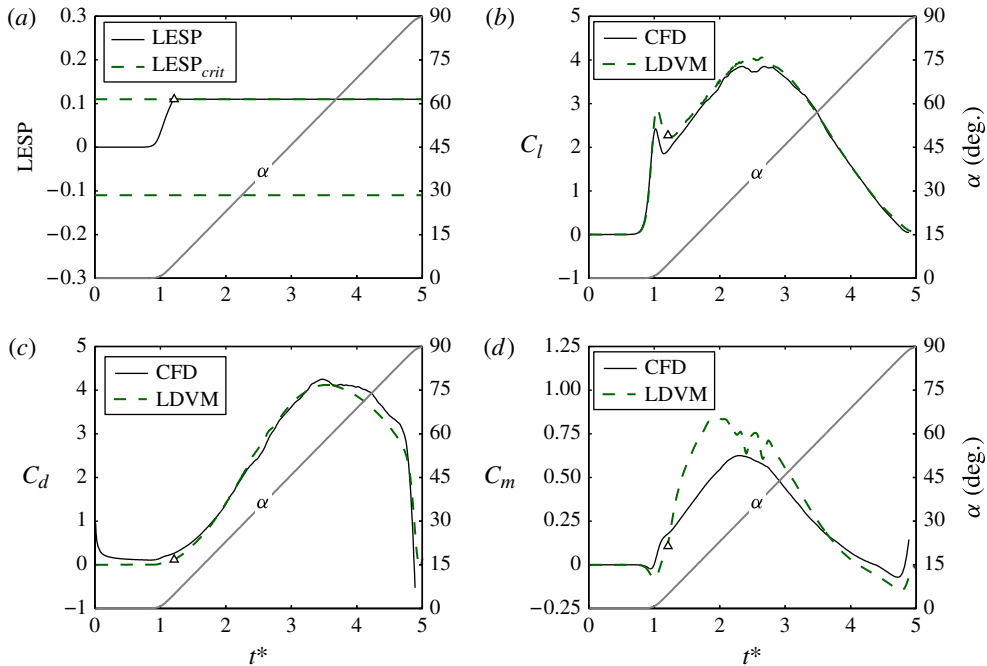


FIGURE 22. (Colour online) Case study 5A (flat plate, $Re = 1000$): LESP and loads. Variation with $t^* = tU/c$ of: (a) LESP from LDVM, (b) lift coefficient from LDVM and CFD, (c) drag coefficient from LDVM and CFD, (d) pitching-moment coefficient about the half chord from LDVM and CFD. The CFD solutions are from Wang & Eldredge (2013). The initiation and termination of LEV shedding is marked on the LDVM curves using open and filled triangles respectively, with upward/downward-pointing triangles indicating upper/lower-surface LEV shedding. The right-hand axes show the scale for pitch-angle variation, $\alpha(t^*)$.

when $\alpha = 90^\circ$ is reached. Details of the motion are provided in appendix B, and the pitch-angle variation is plotted in figure 22. This motion is labelled case 5A.

Figure 22(a) shows the time variation of the LESP. We see that the LESP increases with pitch angle until it reaches the positive critical value of $+0.11$ at t^* of approximately 1.2 and pitch angle of approximately 5° . After this time, the LESP is constrained to the critical value by shedding of clockwise discrete vortices at every time step. These discrete vortices form an LEV that sheds from the aerofoil upper surface, and this LEV grows until the end of the motion at $t^* = 5.0$. Figure 23 compares the flow predictions from the LDVM and from CFD. The formation and growth of the LEV and the TEV shedding from the LDVM are seen to compare excellently with CFD results. Figure 22(b–d) compares the predictions of lift, drag and pitching-moment (about half-chord) coefficients from the two methods. The lift and drag from the LDVM are seen to be in excellent agreement with CFD; the discrepancies in the C_m prediction are attributed to the thick viscous layers adjacent to the upper surface of the plate, visible in the CFD vorticity plots in figure 23, that are not modelled in the LDVM.

The second motion in this case study, labelled case 5B, is a pitch-ramp of amplitude 45° pivoting about the leading edge, with a non-dimensional pitch rate of $K = 0.4$ and smoothing parameter $a = 11$. In this case, the motion is not stopped at the end of the

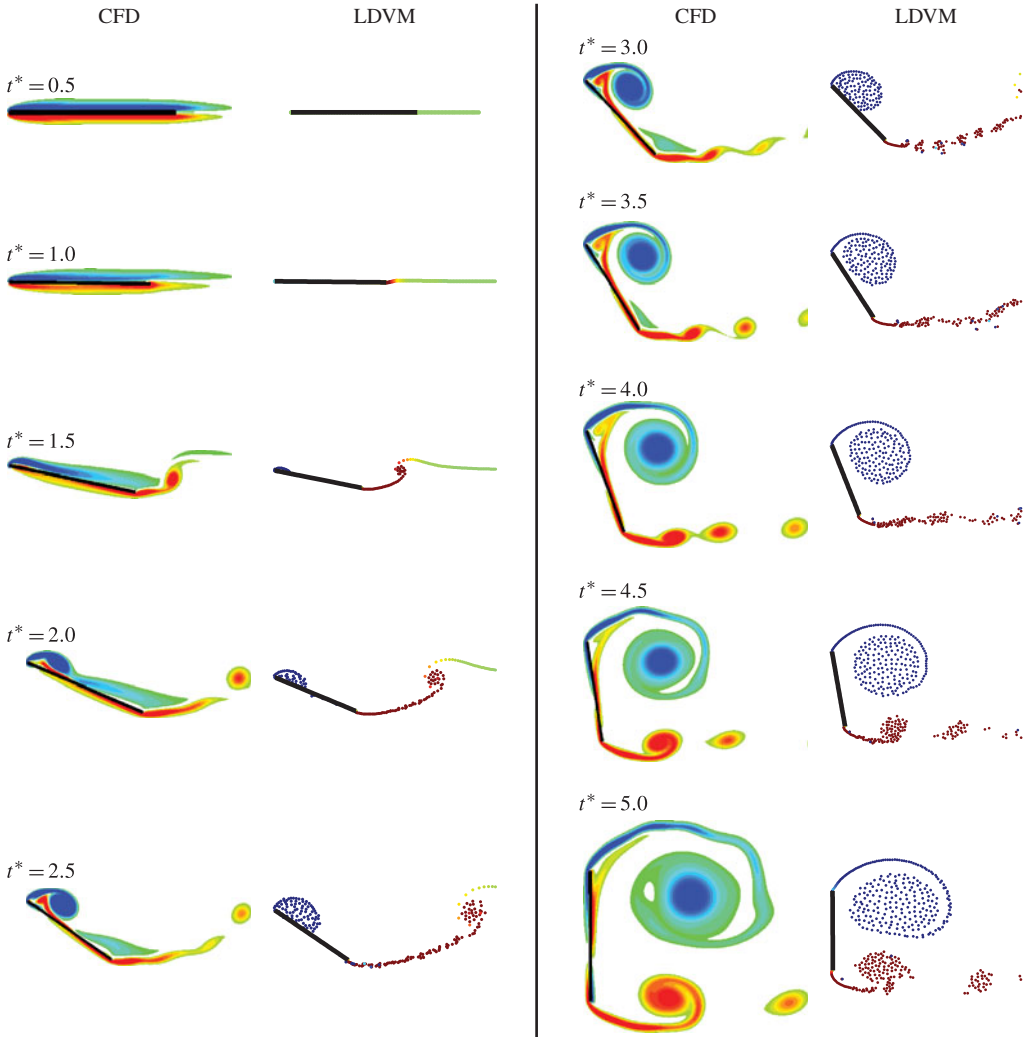


FIGURE 23. (Colour online) Case study 5A (flat plate, $Re = 1000$): flow features. Comparison of flow features between LDVM and CFD of Wang & Eldredge (2013) for t^* from 0.5 to 5.0.

ramp and the plate is made to stay at $\alpha = 45^\circ$ for approximately 7 convective times, with the aim of studying how the vortex shedding evolves with time and whether the results from the LDVM agree with those from CFD during this shedding process. Details of the motion are provided in appendix B, and the pitch-angle variation is plotted in figure 24.

We see from figure 24(a) that the LESP rapidly increases with pitch angle and reaches the critical LESP value of 0.11 early in the upstroke. The LESP then stays at the critical value throughout the remainder of the motion. As a consequence, clockwise discrete vortices are shed at every time step from early in the upstroke to the end of the motion. Unlike in case 5A, these discrete vortices do not roll up into one single LEV. Instead, as seen from the flow pictures in figure 25, the LEV builds up in strength until approximately $t^* = 3.5$. At this time the LEV is

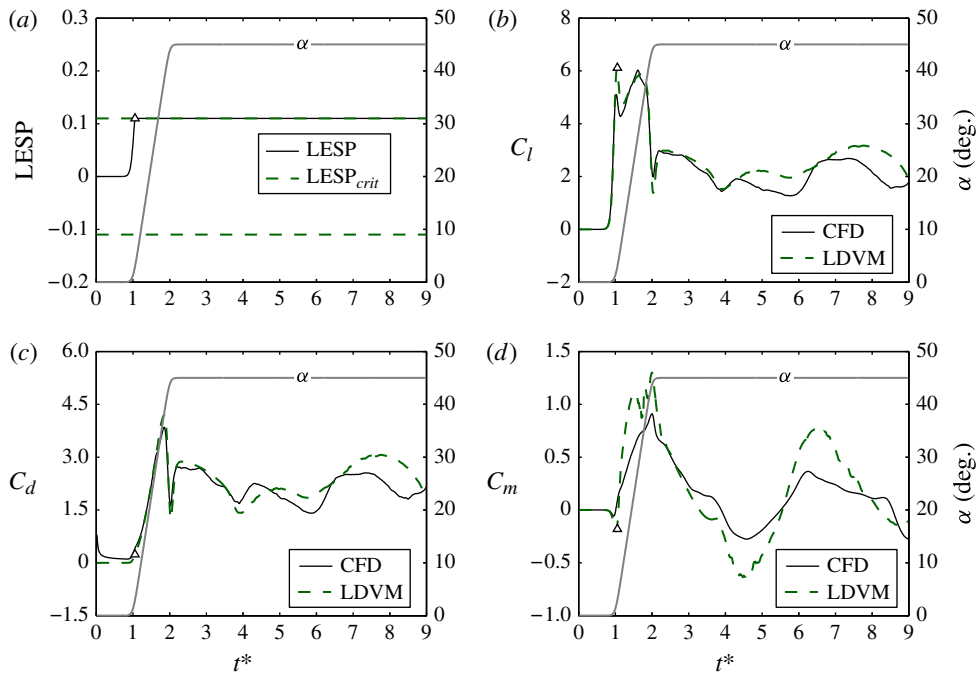


FIGURE 24. (Colour online) Case study 5B (flat plate, $Re = 1000$): LESP and loads. Variation with $t^* = tU/c$ of: (a) LESP from LDVM, (b) lift coefficient from LDVM and CFD, (c) drag coefficient from LDVM and CFD, (d) pitching-moment coefficient about the half chord from LDVM and CFD. The initiation and termination of LEV shedding is marked on the LDVM curves using open and filled triangles respectively, with upward/downward-pointing triangles indicating upper/lower-surface LEV shedding. The right-hand axes show the scale for pitch-angle variation, $\alpha(t^*)$.

of a size large enough to induce the trailing-edge shed vortices to roll up into a concentrated TEV over the aft portion of the upper surface of the aerofoil. When the TEV grows sufficiently large, it causes a detachment of the LEV from the feeding sheet emanating from the leading edge. The flow physics of the LEV detachment has been explained in a recent article by Rival *et al.* (2014), in which the authors show that LEV detachment is initiated when the rear stagnation point aft of the LEV on the upper surface of the aerofoil (half saddle point), reaches the trailing edge. The flow visualisation snapshots from our LDVM and from the CFD results of Eldredge (2007) in figure 25 appear to be in agreement with the explanation of Rival *et al.* (2014). This process alternates, resulting in a von Kármán vortex street. The flow predictions from the LDVM are seen to be in good agreement with the vorticity plots from CFD in figure 25.

Figure 24(b–d) compares the load predictions from LDVM and CFD. The lift and drag results from the two methods are seen to agree well until approximately $t^* = 3.5$, when the alternate LEV/TEV vortex shedding starts. After this time, the results from the two methods have some discrepancies, although their time histories have similar behaviour. As with previous cases, there are discrepancies in the results from LDVM and CFD for the pitching-moment coefficient, which are attributed to the formation of thick boundary layers on the upper surface not modelled in the LDVM.

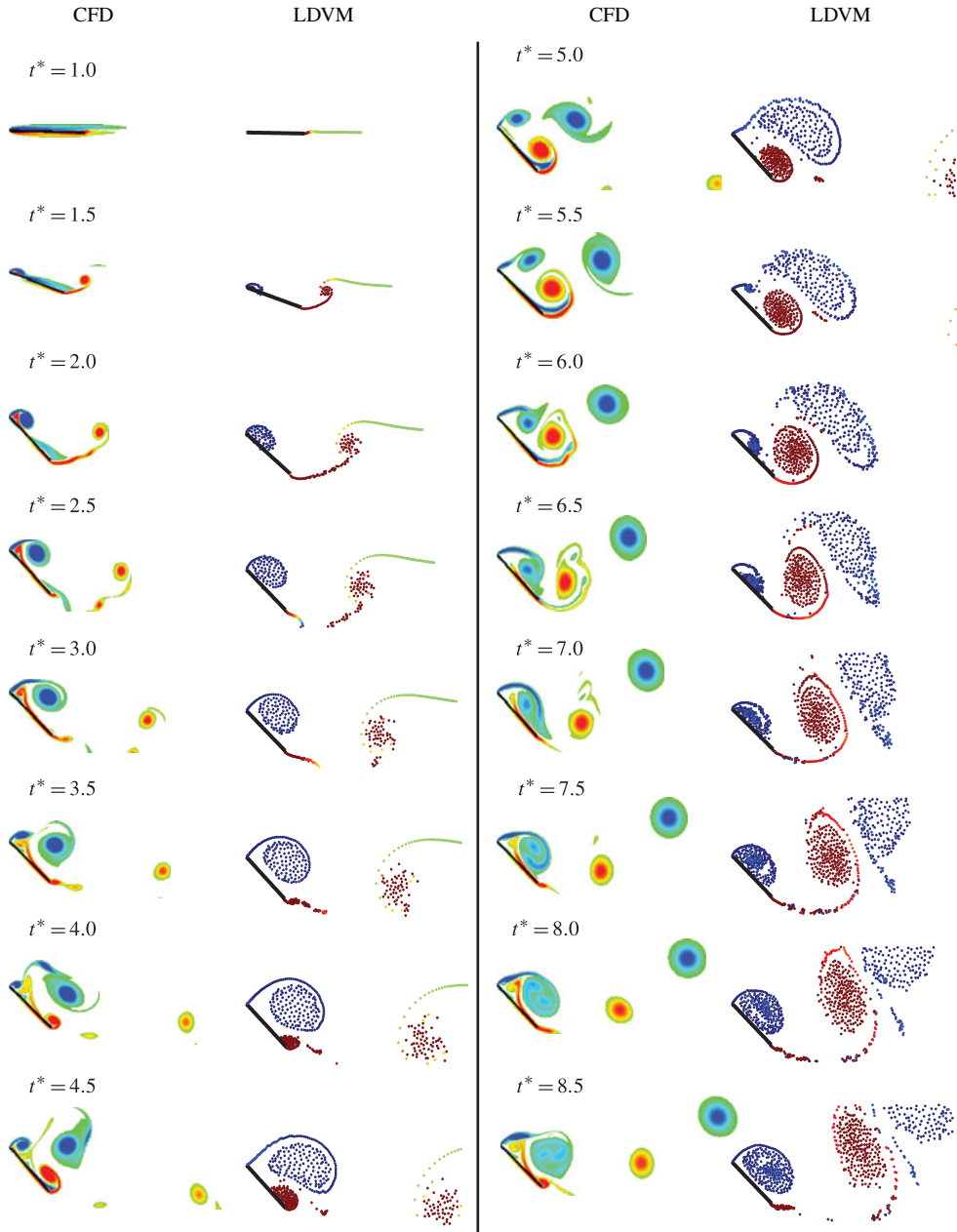


FIGURE 25. (Colour online) Case study 5B (flat plate, $Re = 1000$): flow features. Comparison of flow features between LDVM and CFD of Eldredge (2007) for t^* from 1.0 to 8.5.

4. Limitations of the method and possible extensions

Although the predictions from the current LDVM are in reasonable, and sometimes excellent, agreement with those from CFD and experiments, discrepancies were seen

in all case studies. These were attributed to the formation of thick or separated boundary layers on the aerofoil surfaces, not modelled in the LDVM theory. The current method can be made more generally applicably by developing a low-order approach for modelling the effect of thick/separated boundary layers, perhaps using a dynamically varying camberline through an adaptation of the decambering approach (Mukherjee & Gopalarathnam 2006).

Another disadvantage, which is characteristic of vortex methods, is the exponential increase in computational time with number of vortices in the flow field ($O(n^2)$). Fast summation methods could be used to reduce the computational cost down to $O(n \log n)$ (Barnes & Hut 1986) or $O(n)$ (Carrier, Greengard & Rokhlin 1988). Amalgamation of vortices or deletion of vortices that exit the field of interest could be used to control the vortex count.

We also note that the method presented in this paper is valid only when the free-stream velocity, U , is constant and large compared to the velocities induced at the leading edge due to pitch, plunge, or vortical structures in the flow. When studying perching motions, where U is time varying, or hovering motions, where U is small or zero, this assumption is violated. The main quandary in such situations is in the use of an appropriate Reynolds number for determining the critical LESP. Our recent conference paper (Ramesh *et al.* 2013a) presents an approach to extend the method to perching and hovering situations. The key difference is that the critical-LESP value is determined not for the free-stream Reynolds number, but for a Reynolds number that uses the leading-edge velocity which includes free-stream, motion-induced, and vortex-induced velocity contributions. With such a calibration, the critical LESP for perching and hovering will not be constant during the motion, but will be time variant. Our early results in Ramesh *et al.* (2013a) show that this reformulation successfully extends the current method to motions in which the free stream is time varying or small or zero.

5. Conclusions

Low-order and theoretical methods for unsteady aerofoil flows have been hampered by the lack of a general approach for modelling LEV shedding. We present a theoretical criterion that allows LEV shedding to be modelled in low-order methods. This criterion is based on the argument that, for any given aerofoil leading-edge shape and Reynolds number, there is a maximum limit for the suction that can be supported by the leading edge. This maximum limit is independent of the motion kinematics. We have developed a leading-edge suction parameter, LESP, which is incorporated in a large-angle, discrete-time, arbitrary-motion unsteady thin-aerofoil theory. We show that the A_0 Fourier term of the chordwise variation of bound vorticity in the theory can be used as the LESP. By monitoring the instantaneous value of the LESP at every time step of the motion calculation, LEV formation can be predicted. When the instantaneous LESP is less than the critical value, the flow at the leading edge is attached and there is no LEV shedding. When it exceeds the critical value, vortex shedding takes place at the leading edge. We further postulate that even during the LEV shedding process, the leading-edge suction is limited to the critical value. Thus, as long as the motion and/or the vortical structures in the flow attempt to cause the leading-edge suction to exceed the critical value, the leading edge limits the suction to the critical value by shedding leading-edge vorticity at the appropriate rate.

This general idea has been used to augment the unsteady thin-aerofoil theory with discrete-vortex shedding from the leading edge. At any time step, if the instantaneous

value of the LESP exceeds the pre-determined critical value, then a discrete vortex is shed at the leading edge. The strength of this discrete vortex is determined by the requirement that the LESP is maintained at the critical value, and the direction of the discrete vortex shed at the leading edge is clockwise or counter-clockwise depending on whether the LESP is positive or negative. The discrete vortices are convected with the local velocity like in other discrete-vortex methods. Because the instantaneous LESP is the A_0 Fourier term, which is determined by satisfying the zero-normal-flow boundary condition on the aerofoil, it correctly takes into consideration the effects of the motion kinematics and the flow induced by the vortical structures around the aerofoil. Thus the shedding at any given time instant is also affected by the history of the shedding until that time. When the instantaneous LESP falls below the critical value, then LEV shedding is terminated. The critical LESP value for any aerofoil and Reynolds number is determined empirically using experiment, CFD, or via matching with a force history for a single prototypical motion, and can then be used for any other motion for that aerofoil and Reynolds number. Thus, with the use of a single empirically determined parameter, the critical LESP, the LESP-modulated discrete-vortex method, LDVM, is able to account for the initiation, shedding rate, growth, and termination of intermittent LEVs in an arbitrary unsteady motion. In the authors' experience with this model, deviations in the critical-LESP value of the order of $\pm 10\%$ do not significantly alter the solution obtained. Indeed, this is the justification for using just two significant digits in the critical-LESP values.

The results presented in this paper for a variety of motion kinematics and range of Reynolds numbers show that the predicted forces and flows agree remarkably well with results from high-order CFD and experiments, even though the LDVM takes only a small fraction of the time required by high-order computations. The run times for the LDVM on a single-processor computer are less than 10 min for all motions in this paper, often considerably shorter. In comparison, the high-order computations typically require several hours on a multi-processor computer. Discrepancies between the LDVM results and those from CFD and experiments are attributed to boundary-layer separation on the aerofoil surface, which is not modelled in the current method. Thus, one limitation of the current LDVM is that it is likely to give erroneous predictions when there is significant separation on the aerofoil; such situations can arise when the reduced frequency of motion is small, resulting in trailing-edge stall occurring prior to the occurrence, if any, of LEV formation. The current method can be made more generally applicable by developing a low-order approach for modelling the effect of separated boundary layers. Another disadvantage is the increase in computational time with number of vortices in the flow field as $O(n^2)$. Fast summation methods could be used to bring down the computational cost to $O(n \log n)$ (Barnes & Hut 1986) or $O(n)$ (Carrier *et al.* 1988). Techniques such as amalgamation of vortices or deletion of vortices that exit the field of interest could be employed to control the vortex count. Notwithstanding these limitations, the research presented makes an important contribution by introducing and demonstrating a new criterion for LEV shedding, thus addressing one of the major shortcomings of discrete-vortex methods for unsteady aerofoil flows.

Acknowledgements

The authors wish to gratefully acknowledge the support of the US Air Force Office of Scientific Research through grant FA 9550-10-1-0120 and program manager

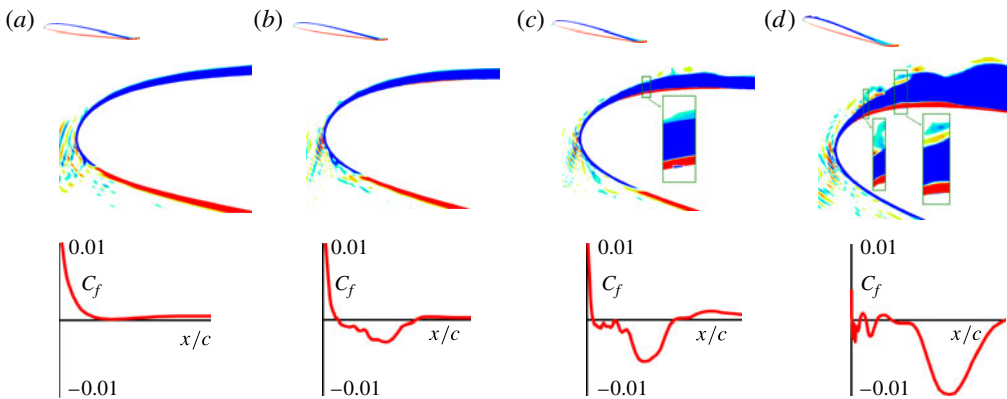


FIGURE 26. (Colour online) Vorticity and upper-surface skin-friction coefficient plots from CFD during the LEV formation process. The choice of subplots (a)–(d) is discussed in the text. The appearance of a positive vorticity region is highlighted.

Dr Douglas Smith. We thank Professor Eldredge of UCLA for sharing results from the couplevm analysis, used in case study 5. We thank Professor Dumas for use of the flow plots from Kinsey & Dumas (2008) in our figures 19 and 21. This article is a revised version of *AIAA Paper 2012–3027*.

Appendix A. Identification of critical LESP from CFD

We present here the procedure that we developed for identifying the critical LESP from CFD (NCSU REACTMB-INS code) skin-friction information, which was used in case studies 1, 2, and 3. For the illustration of this procedure, we consider the formation of a clockwise LEV on the upper surface of an aerofoil undergoing a generic pitch-up motion. This motion is analysed using the LDVM and CFD. The LDVM analysis for this procedure is done using an attached-flow assumption at the leading edge, which is achieved by using as input an artificially high critical-LESP value to disable any discrete-vortex shedding at the leading edge.

The upper-surface skin-friction (C_f) distributions from CFD are examined at various time instants of the motion to identify several key steps that lead to the formation of the LEV. The flow features leading to LEV formation have been discussed by several authors (see Visbal & Shang 1989; Acharya & Metwally 1992; Doligalski, Smith & Walker 1994; Ghosh Choudhuri, Knight & Visbal 1994). Figure 26 shows a series of vorticity and C_f plots for the upper-surface leading-edge region for the aerofoil undergoing the generic pitch-up motion used in this appendix. The four subplots (figures 26a–26d) are used to highlight the following flow features:

- (a) Attached flow: Well before the initiation of the LEV formation, the flow is attached at the leading edge. Vorticity in the attached boundary layer is thin and C_f is positive.
- (b) Onset of reversed flow: LEV formation is first preceded by the formation of a small region of reversed flow near the leading edge of the aerofoil, signalled by the appearance of counter-clockwise vorticity near the surface and a small region of negative C_f .

- (c) Initiation of LEV formation: Next, a small region of clockwise vorticity starts to develop at the surface within the region of counter-clockwise vorticity seen in (b). This flow feature is manifested as spikes in the negative- C_f distribution that reach up to zero and subsequently become one or more regions of positive C_f within the regions of negative- C_f distribution. This flow feature signals the formation of the shear layer in which there is an eruption of surface flow into the main stream. In our work, we take the instant when the spikes in the negative- C_f region first reach the zero value as the time corresponding to the initiation of LEV formation. We have used this C_f condition as a quantitative way to consistently identify the time instant of LEV initiation. The LESP value from the LDVM analysis corresponding to this time instant is taken as the critical-LESP value for this aerofoil, motion, and Reynolds number. As shown in § 2.1.2, the critical-LESP value for a given aerofoil and Reynolds number is independent of motion kinematics.
- (d) Formation and feeding of the LEV: The eruption of surface flow, initiated in (c), results in a plume of clockwise vorticity flowing into the main stream. During these time instants, there are several spikes in the C_f distribution corresponding to positive- C_f regions embedded within a larger negative- C_f region.

Appendix B. List of motion kinematics, critical-LESP values and LDVM run times

The motion kinematics employed in § 3, the critical-LESP values used in the different case studies, and the simulation run times for the LDVM are listed in table 2.

The smoothed ramp–hold–return motion used in this paper is generated using Eldredge’s canonical formulation (Eldredge *et al.* 2009; Wang & Eldredge 2013). A smoothing function, $G(t)$, is defined as:

$$G(t) = \ln \left[\frac{\cosh(aU_\infty(t - t_1)/c) \cosh(aU_\infty(t - t_4)/c)}{\cosh(aU_\infty(t - t_2)/c) \cosh(aU_\infty(t - t_3)/c)} \right] \tag{B 1}$$

where a is a free parameter that determines the smoothing at corners and the times t_1 to t_4 are: $t_1 =$ time from reference 0 until start of ramp; $t_2 = t_1 + A/2K$; $t_3 = t_2 + \pi A/4K - A/2K$; $t_4 = t_3 + A/2K$ where A is the amplitude of pitch (in radians) or plunge, and K is the non-dimensional pitch/plunge rate. The smoothed pitch/plunge history over the ramp–hold–return motion is given by:

$$\alpha(t) / \frac{h}{c}(t) = A \frac{G(t)}{\max(G(t))}. \tag{B 2}$$

The sinusoidal motion kinematics employed in §§ 3.3 and 3.4 are generated as:

$$\frac{h}{c}(t) = \left(\frac{h}{c} \right)_{\max} \cos(2\pi f t), \tag{B 3}$$

$$\alpha(t) = \alpha_{\text{mean}} + \alpha_{\max} \cos(2\pi f t + \phi) \tag{B 4}$$

where $(h/c)_{\max}$ and α_{\max} are the plunge and pitch amplitudes, f is frequency of the sinusoids, and ϕ is the phase between pitch and plunge. The reduced frequency for sinusoidal motions is defined as $k = (2\pi f)c/2U$, which provides the ratio between convective time, $t_c = c/U$, and time period, $T = 1/f$, as $t_c/T = k/\pi$.

Case study	Kinematics	Aerofoil	Re	LESP _{crit}	Run time (s)
1	Eldredge function: $\alpha_{max} = 25$ $K = 0.11$ $a = 11$ Pivot – LE	SD7003	30 000	0.18	14
2	Eldredge function: $\alpha_{max} = 90$ $K = 0.4$ $a = 2$ Pivot – TE	SD7003	100 000	0.14	34
3	A. Sinusoid: $\alpha_{mean} = 4^\circ$ $\alpha_{max} = 22.5^\circ$ $h/c_{max} = 0.05$ $k_\alpha = k_h = 3.93$ $\phi = 90^\circ$ Pivot – 1/4 chord	SD7003	10 000	0.21	8 (1 cycle) 60 (2 cycles) 201 (3 cycles)
	B. Sinusoid: $\alpha_{mean} = 4^\circ$ $\alpha_{max} = 0$ $h/c_{max} = 0.5$ $k_h = 0.393$	SD7003	10 000	0.21	20 (1 cycle) 160 (2 cycles) 533 (3 cycles)
	C. Sinusoid: $\alpha_{mean} = 4^\circ$ $\alpha_{max} = 19.9^\circ$ $h/c_{max} = 0.5$ $k_\alpha = k_h = 0.393$ $\phi = 69.8^\circ$ Pivot – 1/4 chord	SD7003	10 000	0.21	14 (1 cycle) 109 (2 cycles) 365 (3 cycles)
4	Sinusoid: $\alpha_{mean} = 0$ $\alpha_{max} = 76.33^\circ$ $h/c_{max} = 1.0$ $k_\alpha = k_h = 0.377$ $\phi = 90^\circ$ Pivot – 1/3 chord	NACA 0015	1100	0.19	18 (1 cycle) 140 (2 cycles) 469 (3 cycles)
5	A. Eldredge function: $\alpha_{max} = 90$ $K = 0.2$ $a = 11$ Pivot – LE	Flat plate	1000	0.11	16
	B. Eldredge function: $\alpha_{max} = 45$ $K = 0.4$ $a = 11$ Pivot – LE	Flat plate	1000	0.11	63

TABLE 2. Table of motion kinematics, critical-LESP values and LDVM run times. The run times are from a standard single-processor desktop computer. In comparison, the high-order CFD methods in all five case studies typically require several hours of run time on multiple processors.

REFERENCES

- ABBOTT, I. H. & VON DOENHOFF, A. E. 1959 *Theory of Wing Sections*. Dover.
- ACHARYA, M. & METWALLY, M. H. 1992 Unsteady pressure field and vorticity production over a pitching airfoil. *AIAA J.* **30** (2), 403–411.
- ANSARI, S. A., ŻBIKOWSKI, R. & KNOWLES, K. 2006a Nonlinear unsteady aerodynamic model for insect-like flapping wings in the hover. Part 1: methodology and analysis. *Proc. Inst. Mech. Engrs G* **220** (2), 61–83.
- ANSARI, S. A., ŻBIKOWSKI, R. & KNOWLES, K. 2006b Nonlinear unsteady aerodynamic model for insect-like flapping wings in the hover. Part 2: implementation and validation. *Proc. Inst. Mech. Engrs G* **220** (3), 169–186.
- BAIK, Y. S., BERNAL, L. P., GRANLUND, K. & OL, M. V. 2012 Unsteady force generation and vortex dynamics of pitching and plunging airfoils. *J. Fluid Mech.* **709**, 37–68.
- BARNES, J. & HUT, P. 1986 A hierarchical $O(N \log N)$ force-calculation algorithm. *Nature* **324**, 446–449.
- BEDDOES, T. S. 1978 Onset of leading-edge separation effects under dynamic conditions and low Mach number. In *34th Annual Forum of the American Helicopter Society*, vol. 17.
- BRUNTON, S. L., ROWLEY, C. W. & WILLIAMS, D. R. 2013 Reduced-order unsteady aerodynamic models at low Reynolds numbers. *J. Fluid Mech.* **724**, 203–233.
- BRYANT, M., GOMEZ, J. C. & GARCIA, E. 2013 Reduced-order aerodynamic modelling of flapping wing energy harvesting at low Reynolds number. *AIAA J.* **51** (12), 2771–2782.
- CARR, L. W. 1988 Progress in analysis and prediction of dynamic stall. *J. Aircraft* **25** (1), 6–17.
- CARR, L. W., PLATZER, M. F., CHANDRASEKHARA, M. S. & EKATERINARIS, J. 1990 Experimental and computational studies of dynamic stall. In *Numerical and Physical Aspects of Aerodynamic Flows IV* (ed. T. Cebeci), pp. 239–256. Springer.
- CARRIER, J., GREENGARD, L. & ROKHLIN, V. 1988 A fast adaptive multipole algorithm for particle simulations. *SIAM J. Sci. Stat. Comput.* **9** (4), 669–686.
- CASSIDY, D. A., EDWARDS, J. R. & TIAN, M. 2009 An investigation of interface-sharpening schemes for multi-phase mixture flows. *J. Comput. Phys.* **228** (16), 5628–5649.
- CHANDRASEKHARA, M. S., AHMED, S. & CARR, L. W. 1990 Schlieren studies of compressibility effects on dynamic stall of aerofoils in transient motion. *AIAA Paper* 90-3038.
- CHANDRASEKHARA, M. S., AHMED, S. & CARR, L. W. 1993 Schlieren studies of compressibility effects on dynamic stall of transiently pitching aerofoils. *J. Aircraft* **30** (2), 213–220.
- CHOI, J.-I. & EDWARDS, J. R. 2008 Large eddy simulation and zonal modelling of human-induced contaminant transport. *Indoor Air* **18** (3), 233–249.
- CHOI, J.-I. & EDWARDS, J. R. 2012 Large-eddy simulation of human-induced contaminant transport in room compartments. *Indoor Air* **22** (1), 77–87.
- CHOI, J.-I., OBEROI, R. C., EDWARDS, J. R. & ROSATI, J. A. 2007 An immersed boundary method for complex incompressible flows. *J. Comput. Phys.* **224** (2), 757–784.
- CHORIN, A. J. 1973 Numerical study of slightly viscous flow. *J. Fluid Mech.* **57** (4), 785–796.
- CLEMENTS, R. R. 1973 An inviscid model of two-dimensional vortex shedding. *J. Fluid Mech.* **57** (2), 321–336.
- CLEMENTS, R. R. & MAULL, D. J. 1975 The representation of sheets of vorticity by discrete vortices. *Prog. Aerosp. Sci.* **16** (2), 129–146.
- DOLIGALSKI, T. L., SMITH, C. R. & WALKER, J. D. A. 1994 Vortex interactions with walls. *Annu. Rev. Fluid Mech.* **26** (1), 573–616.
- EDWARDS, J. R. & CHANDRA, S. 1996 Comparison of eddy viscosity – transport turbulence models for three-dimensional, shock-separated flowfields. *AIAA J.* **34** (4), 756–763.
- EKATERINARIS, J. A. & PLATZER, M. F. 1998 Computational prediction of aerofoil dynamic stall. *Prog. Aerosp. Sci.* **33** (11–12), 759–846.
- ELDRIDGE, J. D. 2007 Numerical simulation of the fluid dynamics of 2D rigid body motion with the vortex particle method. *J. Comput. Phys.* **221** (2), 626–648.
- ELDRIDGE, J. D., WANG, C. J. & OL, M. V. 2009 A computational study of a canonical pitch-up, pitch-down wing maneuver. *AIAA Paper* 2009-3687.

- EVANS, W. T. & MORT, K. W. 1959 Analysis of computed flow parameters for a set of sudden stalls in low speed two-dimensional flow. *NACA TN D-85*.
- GARMANN, D. J. & VISBAL, M. R. 2011 Numerical investigation of transitional flow over a rapidly pitching plate. *Phys. Fluids* **23**, 094106.
- GARRICK, I. 1937 Propulsion of a flapping and oscillating aerofoil. *NACA Rep.* 567.
- GHOSH CHOUDHURI, P., KNIGHT, D. & VISBAL, M. R. 1994 Two-dimensional unsteady leading-edge separation on a pitching aerofoil. *AIAA J.* **32** (4), 673–681.
- GRANLUND, K., OL, M. V. & BERNAL, L. 2011 Experiments on pitching plates: force and flowfield measurements at low Reynolds numbers. *AIAA Paper* 2011-0872.
- GRANLUND, K., OL, M. V. & BERNAL, L. P. 2013 Unsteady pitching flat plates. *J. Fluid Mech.* **733**, R5.
- HALD, O. H. 1979 Convergence of vortex methods for Euler's equations, II. *SIAM J. Numer. Anal.* **16** (5), 726–755.
- HAMMER, P., ALTMAN, A. & EASTEP, F. 2014 Validation of a discrete vortex method for low Reynolds number unsteady flows. *AIAA J.* **52** (3), 643–649.
- JONES, K. D. & PLATZER, M. F. 1997 A fast method for the prediction of dynamic stall onset on turbomachinery blades. *ASME Paper* 97-GT-101.
- VON KÁRMÁN, T. & BURGERS, J. M. 1963 *General Aerodynamic Theory – Perfect Fluids* (ed. W. F. Durand), Aerodynamic Theory: A General Review of Progress, vol. 2. Dover.
- VON KÁRMÁN, T. & SEARS, W. 1938 Aerofoil theory for non-uniform motion. *J. Aeronaut. Sci.* **5** (10), 379–390.
- KATZ, J. 1981 Discrete vortex method for the non-steady separated flow over an aerofoil. *J. Fluid Mech.* **102**, 315–328.
- KATZ, J. & PLOTKIN, A. 2000 *Low-Speed Aerodynamics*. Cambridge University Press.
- KINSEY, T. & DUMAS, G. 2008 Parametric study of an oscillating aerofoil in a power-extraction regime. *AIAA J.* **46** (6), 1318–1330.
- KIYA, M. & ARIE, M. 1977 A contribution to an inviscid vortex-shedding model for an inclined flat plate in uniform flow. *J. Fluid Mech.* **82** (2), 241–253.
- KRIST, S. L., BIEDRON, R. T. & RUMSEY, C. L. 1998 CFL3D user's manual. *NASA TM* 208444.
- LEISHMAN, J. G. 2002 *Principles of Helicopter Aerodynamics*. Cambridge University Press.
- LEONARD, A. 1980 Vortex methods for flow simulation. *J. Comput. Phys.* **37** (3), 289–335.
- MCAVOY, C. W. & GOPALARATHNAM, A. 2002 Automated cruise flap for aerofoil drag reduction over a large lift range. *J. Aircraft* **39** (6), 981–988.
- MCCROSKEY, W. J. 1981 The phenomenon of dynamic stall. *NASA TM* 81264.
- MCCROSKEY, W. J. 1982 Unsteady aerofoils. *Annu. Rev. Fluid Mech.* **14**, 285–311.
- MCCUNE, J. E., LAM, C. G. & SCOTT, M. T. 1990 Nonlinear aerodynamics of two-dimensional airfoils in severe maneuver. *AIAA J.* **28** (3), 385–393.
- MCGOWAN, G. Z., GRANLUND, K., OL, M. V., GOPALARATHNAM, A. & EDWARDS, J. R. 2011 Investigations of lift-based pitch-plunge equivalence for airfoils at low Reynolds numbers. *AIAA J.* **49** (7), 1511–1524.
- MORRIS, W. J. & RUSAK, Z. 2013 Stall onset on aerofoils a low to moderately high Reynolds number flows. *J. Fluid Mech.* **733**, 439–472.
- MUKHERJEE, R. & GOPALARATHNAM, A. 2006 Poststall prediction of multiple-lifting-surface configurations using a decambering approach. *J. Aircraft* **43** (3), 660–668.
- OL, M. V., BERNAL, L., KANG, C. K. & SHYY, W. 2009a Shallow and deep dynamic stall for flapping low Reynolds number airfoils. *Exp. Fluids* **46** (5), 883–901.
- OL, M. V., MCAULIFFE, B. R., HANFF, E. S., SCHOLZ, U. & KAEHLER, C. 2005 Comparison of laminar separation bubble measurements on a low Reynolds number aerofoil in three facilities. *AIAA Paper* 2005-5149.
- OL, M. V., REEDER, M., FREDBERG, D., MCGOWAN, G. Z., GOPALARATHNAM, A. & EDWARDS, J. R. 2009b Computation vs. experiment for high-frequency low-Reynolds number aerofoil plunge. *Intl J. Micro Air Veh.* **1** (2), 99–119.
- PITT FORD, C. W. & BABINSKY, H. 2013 Lift and the leading-edge vortex. *J. Fluid Mech.* **720**, 280–313.

- RAMESH, K. 2013 Theory and low-order modelling of unsteady aerofoil flows. PhD thesis, North Carolina State University, Raleigh, NC.
- RAMESH, K., GOPALARATHNAM, A., EDWARDS, J. R., GRANLUND, K. & OL, M. V. 2013 *textita* Theoretical analysis of perching and hovering maneuvers. *AIAA Paper* 2013-3194.
- RAMESH, K., GOPALARATHNAM, A., EDWARDS, J. R., OL, M. V. & GRANLUND, K. 2013*b* An unsteady aerofoil theory applied to pitching motions validated against experiment and computation. *Theor. Comput. Fluid Dyn.* **27** (6), 843–864.
- RAMESH, K., GOPALARATHNAM, A., OL, M. V., GRANLUND, K. & EDWARDS, J. R. 2011 Augmentation of inviscid aerofoil theory to predict and model 2D unsteady vortex dominated flows. *AIAA Paper* 2011-3578.
- RIVAL, D. E., KRIEGSEIS, J., SCHAUB, P., WIDMANN, A. & TROPEA, C. 2014 Characteristic length scales for vortex detachment on plunging profiles with varying leading-edge geometry. *Exp. Fluids* **55** (1), 1–8.
- ROSENHEAD, L. 1932 The point vortex approximation of a vortex sheet. *Proc. R. Soc. Lond. A* **134**, 170–192.
- SAFFMAN, P. G. & BAKER, G. R. 1979 Vortex interactions. *Annu. Rev. Fluid Mech.* **11** (1), 95–121.
- SARPKAYA, T. 1975 An inviscid model of two-dimensional vortex shedding for transient and asymptotically steady separated flow over an inclined plate. *J. Fluid Mech.* **68** (1), 109–128.
- SELIG, M. S., DONOVAN, J. F. & FRASER, D. B. 1989 *Airfoils at Low Speeds*, Soartech, vol. 8. SoarTech Publications.
- SPALART, P. R. & ALLMARAS, S. R. 1992 A one-equation turbulence model for aerodynamic flows. *AIAA Paper* 92-0439.
- THEODORSEN, T. 1931 On the theory of wing sections with particular reference to the lift distribution. *NASA Tech. Rep.* 383.
- THEODORSEN, T. 1935 General theory of aerodynamic instability and the mechanism of flutter. *NACA Rep.* 496.
- VATISTAS, G. H., KOZEL, V. & MIH, W. C. 1991 A simpler model for concentrated vortices. *Exp. Fluids* **11** (1), 73–76.
- VISBAL, M. R. & SHANG, J. S. 1989 Investigation of the flow structure around a rapidly pitching aerofoil. *AIAA J.* **27** (8), 1044–1051.
- WAGNER, H. 1925 Über die Entstehung des dynamischen Auftriebes von Tragflügeln. *Z. Angew. Math. Mech.* **5** (1), 17–35.
- WANG, C. & ELDREDGE, J. D. 2013 Low-order phenomenological modelling of leading-edge vortex formation. *Theor. Comput. Fluid Dyn.* **27** (5), 577–598.
- XIA, X. & MOHSENI, K. 2013 Lift evaluation of a two-dimensional pitching flat plate. *Phys. Fluids* **25** (091901), 1–26.
- YOUNG, J., ASHRAF, M. A., LAI, J. C. S. & PLATZER, M. F. 2013 Numerical simulation of fully passive flapping foil power generation. *AIAA J.* **51** (11), 2727–2739.
- YOUNG, J., LAI, J. C. S. & PLATZER, M. F. 2014 A review of progress and challenges in flapping foil power generation. *Prog. Aerosp. Sci.* **67**, 2–28.
- ZHU, Q. 2011 Optimal frequency for flow energy harvesting of a flapping foil. *J. Fluid Mech.* **675**, 495–517.